



HAL
open science

Synthesis of alkyl-branched fatty acids by isomerization on micro-mesoporous ferrierite-based zeolitic materials

Jonathan Fabian Sierra-Cantor, Olinda Gimello, Carlos-Alberto Guerrero-Fajardo, Francesco Di Renzo, Hugo Petitjean, Maxime Riviere, Corine Gérardin, Nathalie Tanchoux

► To cite this version:

Jonathan Fabian Sierra-Cantor, Olinda Gimello, Carlos-Alberto Guerrero-Fajardo, Francesco Di Renzo, Hugo Petitjean, et al.. Synthesis of alkyl-branched fatty acids by isomerization on micro-mesoporous ferrierite-based zeolitic materials. *Applied Catalysis B: Environmental*, 2024, 344, pp.123602. 10.1016/j.apcatb.2023.123602 . hal-04619948

HAL Id: hal-04619948

<https://hal.science/hal-04619948>

Submitted on 21 Jun 2024

HAL is a multi-disciplinary open access archive for the deposit and dissemination of scientific research documents, whether they are published or not. The documents may come from teaching and research institutions in France or abroad, or from public or private research centers.

L'archive ouverte pluridisciplinaire **HAL**, est destinée au dépôt et à la diffusion de documents scientifiques de niveau recherche, publiés ou non, émanant des établissements d'enseignement et de recherche français ou étrangers, des laboratoires publics ou privés.

1 **SYNTHESIS OF ALKYL-BRANCHED FATTY ACIDS BY ISOMERIZATION ON MICRO-**
2 **MESOPOROUS FERRIERITE-BASED ZEOLITIC MATERIALS**

3 *Jonathan Fabian Sierra-Cantor*^{a,1}, *Olinda Gimello*^a, *Carlos-Alberto Guerrero-Fajardo*^b, *Francesco*
4 *Di Renzo*^a, *Hugo Petitjean*^a, *Maxime Riviere*^{a,2}, *Corine Gérardin*^{a*}, *Nathalie Tanchoux*^{a*}.

5
6 ^a Institut Charles Gerhardt, Université de Montpellier, CNRS, ENSCM, Montpellier, France

7 ^b Department of Chemistry, Universidad Nacional de Colombia, Aprovechamiento Energético de
8 Recursos Naturales, Carrera 30 45-03, Bogotá, Colombia

9 * Corresponding authors. E-mail addresses: corine.gerardin@enscm.fr, nathalie.tanchoux@enscm.fr.
10 Full postal address: ICGM, Pôle Chimie Balard Recherche, 1919 route de Mende 34293 Montpellier
11 Cedex 5, France.

12 ¹ Present address of J.F. Sierra Cantor: Institut de Chimie des Milieux et Matériaux de Poitiers (IC2MP),
13 Université de Poitiers, CNRS, UMR 7285, 4 Rue Michel Brunet, TSA 51106, F-86073 Poitiers 9, France

14 ² Present address of M. Rivière: VINCI TECHNOLOGIES, 27B Rue du Port - Parc de l'île, 92022 Nanterre

15 **KEYWORDS**

16 Hierarchically porous ferrierite / Fatty acids isomerization / Continuous flow process / reaction
17 mechanism / catalyst deactivation

18
19 **ABSTRACT**

20 The synthesis of alkyl-branched fatty acid methyl esters from fatty acids is of great interest to
21 synthesize high value-added products. The isomerization reaction catalyzed by microporous zeolites is
22 promising due to its high yields, but rapid deactivation is its main drawback. In this work, a
23 micromesoporous ferrierite synthesized by a well-controlled alkaline recrystallization process, was
24 evaluated as a catalyst in the isomerization of methyl oleate. Recrystallized materials present improved
25 accessibility of acid sites at the mouth of 10-MR pores due to the increase of the mesopore surface.
26 Methyl oleate isomerization has been implemented in batch conditions and in a continuous flow
27 process with experiments lasting more than 3 days. Stable yield of branched isomers higher than 50%
28 was reached at 285 °C and 3.5 h⁻¹ WHSV. The catalytic results, combined with a detailed analysis of
29 fresh and spent catalysts, has provided information on the phenomena involved, in particular
30 deactivation.

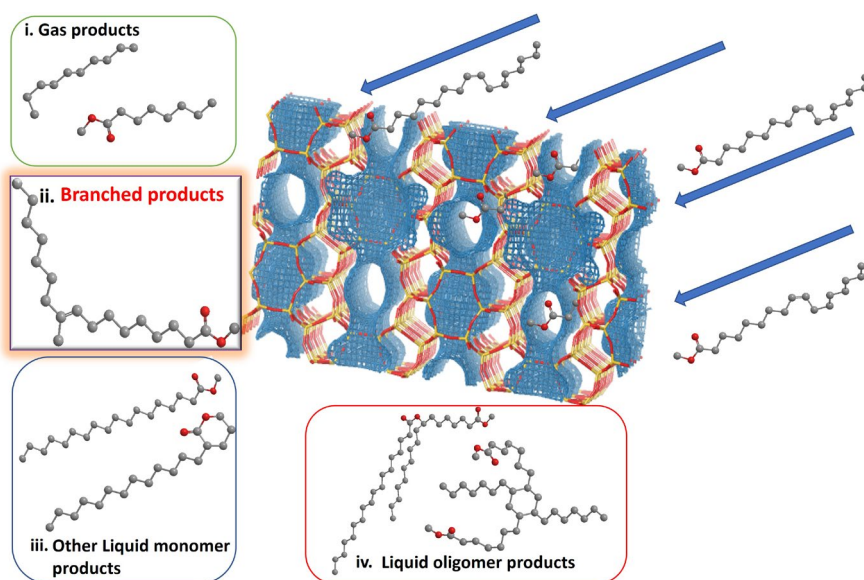
31
32 **1. INTRODUCTION**

33 Interest in lipid biomass as a renewable substitute for fossil oil supply has increased in recent years
34 [1,2]. Among them, the production of vegetable oils increased by 40% between 2010 and 2020,
35 reaching values around 208 Mt/year [3], with a further increase of more than 20% expected in the
36 coming years [4]. Although about 77 % of these oils are used for food production, biofuels, and
37 oleochemical production represent an important part of this demand [4]. In addition to their general

1 uses, they have been used to produce biofuels and other high-value oleochemical products[5]. They
2 have been identified as precursors of high-value products such as biodegradable and biosafe
3 fungicides, surfactants, monomers, plasticizer additives, cosmetics, personal care products, lubricants,
4 etc [1,4–6].

5 In this context, different routes have been investigated for obtaining biodiesel [7], renewable diesel
6 [8], or biolubricants [5] from vegetable oils [9] using porous acidic materials as catalysts [10]. Among
7 them, the isomerization of fatty acids to branched chain fatty acids has attracted attention in recent
8 years. It has resulted in obtaining branched molecules with improved physicochemical properties
9 [11,12]: higher solubility, better water tolerance, oxidative stability [13], lower melting/freezing points,
10 lower viscosity as well as good spreadability, among others [5,14–18]. With this in mind, they have
11 been used as limiting additives in biodegradable lubricants [5,19], as emollients in personal care
12 products [14,20,21], and more recently as additives to improve the cold flow properties of biodiesel
13 [22–24].

14 These alkyl-branched fatty acids are obtained by the isomerization reaction, a complex reaction (see
15 Fig. 1), which can lead to rapid deactivation of the porous acidic catalyst. This reaction is mediated by
16 the rearrangement of a carbenium ion. This step is followed by a skeletal rearrangement in which chain
17 propagation of the carbenium ion onto the hydrocarbon chain of the fatty acid moiety can form
18 multiple double bond positional isomers, cis/trans isomers as well as positional isomers of the
19 branched monoalkyl molecules [23]. In addition, under these pressure and temperature conditions, a
20 large number of by-products can be formed, such as hydroxylated and saturated fatty acids, gamma,
21 and delta lactones, oligomers such as dimers or estolides, as well as products from catalytic cracking
22 [21,25,26]. On the other hand, under these reaction conditions, catalytic β -scission cracking [27] leads
23 to the formation of alkylbenzenes [25] and consequently, it can lead to the formation of carbonaceous
24 deposits formation, which cannot desorb from the active sites, blocking the pores and ultimately
25 deactivating the catalyst [25],[12].



26

27 **Fig. 1.** Reaction of isomerization unsaturated fatty acid methyl esters on porous acid materials: (i.)
28 gas products like light alkanes and volatile fatty acids, (ii.) branched fatty acid methyl esters, (iii.)
29 other liquid monomer products like straight saturated and unsaturated fatty acid methyl esters,
30 gamma and delta lactones, (iv.) Liquid oligomer products such as estolides and dimers

1 With this in mind, several acid porous materials have been tested as catalysts for this reaction [28],
2 materials such as clays (montmorillonite [14,29]), sulfated zirconia with metal promoters, acidic
3 alumina supported noble metals, silica supported phosphotungstic heteropolyacids [30]; and more
4 recently aluminosilicates and silicoaluminophosphates [5,15]. Among them, zeolites have shown a
5 breakthrough performance. Although zeolites with large pores such as mordenite (yield: 66.5%[31])
6 [32], zeolite L (yield: 51%[33]), and β -zeolite (yield: 50% [23,34,35]) have been tested, the real
7 breakthrough came from the use of a zeolite with smaller pore size, ferrierite. Yields up to 74% in
8 branched chain fatty acids were obtained [15,21,31,36]. It was observed that this particular catalytic
9 performance of the zeolites is caused mainly by well-constrained porous network in their ordered
10 structure. The observed high yields were explained by the induced shape selectivity, which limits
11 mainly the oligomerization reactions. The work of Ngo and coworkers showed that the distribution of
12 products depends on the architecture of the channels and the nature of the acidic sites of the zeolites
13 [15,21,31]. However, this well-constrained microporous network leads to a faster loss of catalytic
14 activity of the ferrierite catalysts by coke formation. This is an important drawback for the
15 implementation of zeolite-based catalyst processes for the production of branched chain fatty acids.
16 Various alternatives have been studied to improve catalytic performance of zeolites. The yield of
17 branched chain fatty acids was improved to 87% using bulky Lewis bases as additives [25,30].
18 Treatments with magnesium salts were shown to further reduce the formation of dimers during the
19 reaction [36]. Recently, the presence of intracrystalline mesopores in ferrierite structures has been
20 shown to significantly improve the catalytic performance of the isomerization reaction [37–40].

21 Considering that the presence of these intracrystalline mesopores could help to avoid the losses in
22 their catalytic performance in the isomerization reaction of fatty acids [41,42], this work has analyzed
23 the use of a zeolite with intracrystalline mesopores, previously developed in our research group [43],
24 as a catalyst in this reaction. Considering that this meets the specifications previously described to
25 carry out isomerization reaction on fatty acids, in this work, its performance was compared to parent
26 exchanged ferrierite in methyl oleate isomerization. Their catalytic performance in different conditions
27 of pressure and temperature was compared on a batch and a downstream fixed bed continuous flow
28 reactor to evaluate the effect of the intracrystalline mesopores on the parameters of conversion,
29 selectivity, and time-on-stream stability.

30

31 **2. EXPERIMENTAL SECTION**

32 **2.1 Reagents and materials**

33 Reagent grade oleic acid (91.6 %wt. C18:1; 3.7 % wt. C18:2; 2.6 % wt. C18:0; 1.4 % wt. C16:0; 0.7 % wt.
34 other), sulfuric acid 98%, sodium hydroxide, cetyl Trimethyl Ammonium Bromide (CTAB), heptane,
35 methyl arachidate, and methanol were purchased from Sigma-Aldrich. Na, K-ferrierite (HSZ-720 KOA®
36 Si/Al: 9.2) was purchased from Tosoh Corp.

37 Methyl Oleate was synthesized by acid esterification under reflux at 60°C for 3h with 2% H₂SO₄ and a
38 6:1 molar ratio of oleic acid to methanol. The product was purified by successive washings with water
39 at 40°C followed by vacuum distillation at 60°C. The purity of the methyl esters was checked (ASTM
40 D664) and the content of free fatty acids was lower than 1%.

41 **2.2 Zeolite materials recrystallization and characterization**

1 In a typical synthesis, following the methodology of Cheng *et al.* [43], 4.89 g of Na, K–Ferrierite, and
2 2.49 g of CTAB were mixed with 150 mL of 0.2 M NaOH solution. After stirring for 30 min, the
3 suspension was hydrothermally treated at 130°C in a Teflon-lined stainless-steel autoclave for 72 h.
4 After cooling, the solid was filtered and washed with deionized water until to get pH 7. The product
5 was then dried overnight at 80°C, it was ground, and subjected to ion exchange in 150 mL of a 1.0 M
6 NH₄NO₃ solution for six hours at room temperature. The solid was then filtered, washed, and dried.
7 Later, this NH₄-form ferrierite with CTAB was calcined in an air flow (200 mL/min) in a tube furnace
8 with the following heating program: from room temperature to 550°C with a heating ramp of 120°C/h
9 and a plateau of sixteen hours. The recrystallized ferrierite in the H-form (H-FER-REC) was obtained
10 (mass yield: 65.4%). On the other hand, the ion exchange, drying, and calcination steps were carried
11 out under the same conditions directly on Na, K–Ferrierite to obtain the H-form of the parent zeolite
12 (H-FER-PAR) or simply referred to hereafter as the parent ferrierite.

13 On the one hand, the characterization of the fresh catalyst was as follows. The characterization
14 of the structure, porosity, and composition in these ferrierite materials was carried out according to
15 the characterization methodology of Cheng *et al.* [43]. The crystal structure was analyzed by powder
16 X-ray diffraction (XRD). Data were recorded by continuous scanning in the range of 2 θ values of 0.5 -
17 6° and 4 – 50°. Surface areas and pore volumes were calculated from the analysis of nitrogen
18 adsorption-desorption isotherms recorded at 77 K using a Micromeritics TriStar 3000. The
19 compositions of the samples were determined by elemental analysis using the energy dispersive X-ray
20 (EDS) analysis method on a SEM FEI QUANTA 200F with an accelerating voltage of 15 kV (PT MEA-UM).
21 The particle size and morphology of the materials were evaluated using a SEM HITACHI 4800S (PT IEM)
22 with an accelerating voltage of 5 kV. The distribution, size, and orientation of the intracrystalline
23 mesopores were determined by transmission electron microscopy (TEM) using a JEOL 1200-1400 Plus
24 EXII electron microscope with an accelerating voltage of 100 kV (PT MEA -UM). In addition, ²⁹Si and
25 ²⁷Al Magic Angle Spinning Nuclear Magnetic Resonance (MAS-NMR) analysis of the zeolitic materials
26 was performed on a 300 MHz Varian VNMRS300 spectrometer (UM) using a Varian T3 MAS probe with
27 7.5 mm ZrO₂ rotors. The ²⁹Si MAS NMR spectra were acquired using the quantitative Single Pulse
28 technique with ¹H decoupling with a recycle delay of 60 s, a $\pi/6$ pulse of 2 μ s, and a spin rate of 5 kHz.
29 Q8M8H (octakis(dimethylsiloxo)octasilsesquioxane) was used as a secondary reference (left peak at -
30 2.25 ppm). The spectral window width is 50 kHz and the line broadening is 50 Hz. ²⁷Al MAS NMR spectra
31 were acquired using the quantitative Single Pulse technique with ¹H decoupling with a recycle delay of
32 1 s, a $\pi/6$ pulse of 2 μ s, and a spinning rate of 22 kHz. Aluminum nitrate was used as a secondary
33 reference (peak at 0.0 ppm). The spectral window width is 192 kHz and the line broadening is 50 Hz.
34 Acidic site characterization was performed by temperature programmed desorption of ammonia (TPD-
35 NH₃) to determine the total number of acidic sites and by the infrared analysis of
36 adsorption/desorption analysis of acetonitrile to analyze the different acidic sites. TPD-NH₃ was
37 performed on a Micromeritics AutoChem II® apparatus. Solids (30–50 mg) were calcined in air up to
38 550°C, cooled down to 100°C, and saturated with ammonia. The physisorbed base was swept in a He
39 flow (50 mL/min, 2 h) while the chemisorbed ammonia was desorbed by increasing the temperature
40 (10 °C/min) up to 700°C. Finally, infrared (IR) spectra were recorded on a Bruker EQUINOX 55
41 spectrometer with a DTGS detector in transmission mode. All the IR analyses were performed at room
42 temperature. Infrared analysis of adsorbed CD₃CN (Aldrich, 99.8% D atoms) was performed in a low
43 pressure quartz transmission cell with KBr windows. The catalyst was pressed into a self-supporting
44 wafer (5000 kg.cm⁻², 30 mg, 18 mm in diameter) and then pretreated in the IR cell under a dynamic

1 vacuum (10^{-5} mbar) at 250°C for 16 h before cooling down to room temperature. Deuterated
2 acetonitrile was then adsorbed on the catalyst at an equilibrium pressure of 1.0 mbar. It was then
3 desorbed under a dynamic vacuum for three hours. Four desorption temperatures (25, 50, 100, and
4 150°C) were investigated by increasing the temperature of the catalyst wafer temperature for 15 min.
5 After each desorption treatment, the catalyst was cooled to room temperature before IR
6 measurement. Band areas were computed using Fityk software. The molar density of acid sites was
7 calculated using the Beer-Lambert law and extinction coefficients of $3.60 \text{ cm} \cdot \mu\text{mol}^{-1}$ for Lewis acid sites
8 (2321 cm^{-1}) and $2.05 \text{ cm} \cdot \mu\text{mol}^{-1}$ for Brønsted acid sites ($2306 - 2275 \text{ cm}^{-1}$)[44].

9 On the other hand, the analysis of the washed spent catalytic materials was performed after the
10 removal of soluble impurities. Each stored spent catalytic material (0.5 g) was washed with 10 mL of
11 acetone, centrifuged, and dried at 60°C. A 24-hour Soxhlet treatment with dichloromethane was then
12 performed. The total amount of coke in each sample was determined by thermal gravimetry (TG) using
13 a PerkinElmer TGA 4000. Analyses were performed from 40 °C to 900 °C with a ramp of 5 °C/min in air
14 flow (60 mL/min). The amount of coke was calculated as the sum of mass losses from 250 to 700°C.
15 On the other hand, ^{13}C Cross-Polarization Magic Angle Spinning (CP MAS) NMR analysis was performed
16 on these spent catalytic materials. The spectra were acquired on a 300 MHz Varian VNMR300®
17 spectrometer ("Wide Bore" magnet at 7.05 Tesla). A Varian T3 MAS probe was used with 3.2 mm
18 zirconia rotors and a spinning speed of 12 kHz. Spectra were acquired using the CPMAS technique with
19 a recycle delay of 3 s, a $\pi/2$ pulse of 5 μs , and a contact time of 0.5 ms. The spectral window width was
20 50 kHz, the acquisition time was 40 ms and the line broadening was 50 Hz. Adamantane was used as a
21 secondary reference (left peak at 38.5 ppm).

22 **2.3 Catalytic tests**

23 Isomerization of methyl oleate in batch conditions was carried out with a catalyst loading of 5% wt.,
24 under a N_2 atmosphere, with a reaction time of eight hours, working at temperatures between 260
25 and 285°C and pressures between 2.0 and 4.0 MPa in a 200 mL flange autoclave. The catalytic material
26 (see section 2.2) containing particles of size $<250 \mu\text{m}$ was prepared by compressing the powder at 196
27 MPa, crushing, and sieving it to the desired size. In a typical experiment, 50 g of methyl oleate and 2.5
28 g of the catalytic material were placed in the autoclave and then heated to the desired temperature,
29 which was considered as the starting point of the reaction. After the reaction, the system was cooled
30 down to room temperature and the gas outlet valve was opened to collect gas samples in a cryotrap.
31 After opening the reactor, the reaction mixture was removed and filtered at room temperature. The
32 liquid fraction was sent for GC analyses. The spent catalysts were characterized as described above.
33 The liquid phase extracted from of the two washings with acetone and dichloromethane was analyzed
34 by GC-MS and MALDI-TOF.

35 The isomerization of methyl oleate under continuous flow conditions was carried out in a downstream
36 fixed bed continuous flow reactor (6 mm ID) using 1–1.3 g of catalytic material (see section 2.2) with a
37 particle size in the range of 250 to 425 μm prepared as described above, and mixed with quartz with a
38 particle size ranging in the range of 150 to 250 μm . The amount of quartz was adjusted to keep the
39 total volume of the catalytic bed constant at 3.7 cm^3 . The catalyst was activated *in situ* under a 50
40 mL/min hydrogen flow at 400°C for 18 h (heating rate: 120°C/h). Methyl oleate was pumped at a flow
41 rate of 4.0 ml/h, allowing a W.H.S.V. of 3.5 h^{-1} in the reactor and mixed with the carrier gas (N_2) at the
42 desired pressure (between 2.0 and 4.0 MPa). The reaction temperature varied between 260 and 325°C

1 during the course of a reaction. Lighter gaseous reaction products were analyzed on-line by GC, while
2 liquid fractions were periodically collected for separate analysis (see section 2.4). If the experiment
3 lasted more than one day, the starting material flow was reduced to allow a WHSV of 1.2 h⁻¹ at night.
4 The next day, the flow was normalized to the previous conditions, and the new temperature condition
5 was fixed. This procedure was repeated every day during the course of a typical experiment.

6 **2.4 Analytical method**

7 The products of methyl oleate isomerization form a complex mixture of compounds in the gas and
8 liquid phases due to the complexity of the reaction.

9 The gas fraction products of methyl oleate isomerization were analyzed using a gas chromatograph GC
10 equipped with an FID detector (Agilent 7890A). The chromatographic separation was performed on an
11 Rt-Q-Bond Plot capillary column (30 m x 0.25 mm x 8 μm) coupled in series with an HP-5-ms capillary
12 column (30m x 0.25 mm x 0.25 μm), with hydrogen as the carrier gas.

13 The liquid fraction was analyzed by two different GC methods. For both analyses, samples were
14 prepared by mixing 10 μL of the liquid phase products with 50 μL of internal standard solution (methyl
15 arachidate) and diluting in 1.0 mL of heptane. 1.0 μL of this mixture was injected. The first type of GC
16 analysis was used to determine the amount of oligomers in the samples. The products were analyzed
17 on a GC (Varian 3900) equipped with an HP-5HT[®] capillary column (15 m x 0.32 mm x 0.10 μm). In the
18 second method, all compounds in the liquid fraction (except oligomers) were identified and quantified.
19 Samples were prepared as previously described, and the analysis was performed using a gas
20 chromatograph coupled to a GC-MS mass spectrometer (Shimadzu QP-2010plus). Chromatographic
21 separation was performed on a ZB-FAMES[®] capillary column (60m x 0.25 mm x 0.20 μm).

22 The conversion (C) was defined as $C = 100 \left(1 - \frac{Q_{in-t_i}}{Q_{in-t_0}} \right)$ where Q_{in-t_i} is the concentration of the
23 remaining substrate i at a time i , and Q_{in-t_0} is the initial concentration of the substrate in the starting
24 material. Due to the considerable complexity of the products, they are classified into different families
25 of products in the liquid phase: branched C18 isomer products, linear saturated FAME products
26 (methyl stearate), straight C18 isomers of methyl oleate, cracking products, oligomer, and other
27 products. The yield of a j family of compounds (Y_j) is defined as: $Y_j = 100 \left(\frac{Q_{j-t_i}}{Q_{in-t_0}} \right)$ where Q_{j-t_i} is the
28 concentration of the j kind of compound and Q_{in-t_0} is the concentration of the substrate in the starting
29 material.

30 Oligomers were qualitatively analyzed in the liquid fraction products by MALDI-TOF MS and MS/MS
31 analyses. In addition, the dichloromethane liquid extracts from the Soxhlet procedures of washing of
32 the spent catalysts were also analyzed by the same method. The samples were dissolved in
33 dichloromethane at 5 mg/mL. The matrix used was DHB (2,5-dihydroxybenzoic acid) dissolved at 10
34 mg/mL in acetone. The cationizing agent was lithium chloride (5 mg/mL in acetone). First, 1 μL of LiCl
35 solution was applied to the MALDI plate followed by 0.5 μL of matrix and 0.5 μL of the sample solution.
36 The plate was allowed to dry before analysis. Full scan mass spectra and MS/MS spectra were
37 performed on a Bruker Rapiflex MALDI-TOF/TOF using a nitrogen laser for MALDI ($\lambda=337\text{nm}$). All
38 spectra were acquired in positive ionization mode. Mass spectra from 3000 shots were accumulated
39 for spectra at a 25 kV acceleration voltage and reflectron lens potentials at 26.3 KV. A mixture of

1 peptides was used for external calibration. For the MS/MS mode, the transmission of precursor ions
2 in the collision cell was optimized using an 18 kV deceleration lens and a 2.9 kV MS/MS Pulse.

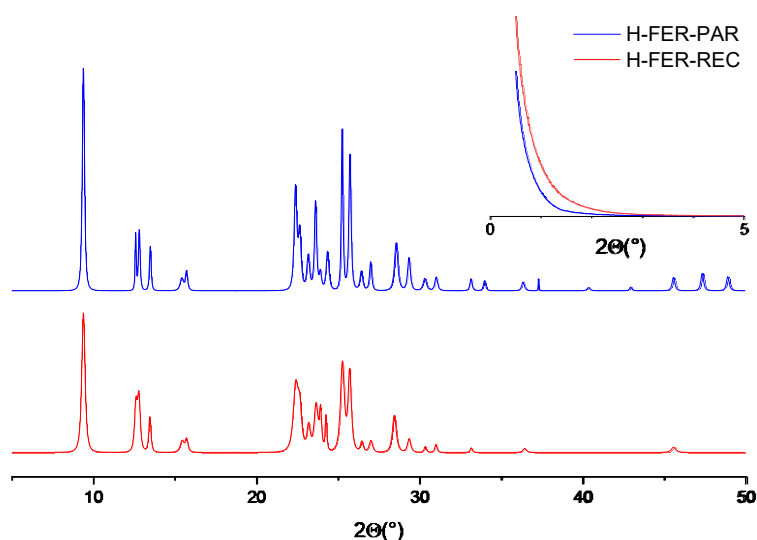
3 Finally, the GC-MS chromatographic analysis of the liquid extracts from spent catalytic materials was
4 performed using the same instrument equipped with an HP-5-ms capillary column (30 m x 0.25 mm x
5 0.25 μm). Each liquid extract was diluted to 1.0 mL of the appropriate solvent (acetone &
6 dichloromethane).

7

8 3. RESULTS AND DISCUSSION

9 3.1 Zeolite Materials recrystallization and characterization

10 Using the recrystallization conditions for highly stable low silica ferrierite established by Cheng *et al.*
11 [43], it was possible to produce a ferrierite-based material that had an added mesopore system and
12 retains its crystalline structure and micropores.



13

14 **Fig. 2.** Powder X-ray diffraction patterns of parent (in blue) and recrystallized (in red) ferrierite
15 materials with magnification of small angle patterns of 0.5-5° of powder X-ray diffraction patterns of
16 parent (H-FER-PAR) and recrystallized (H-FER-REC) ferrierite materials.

17 Fig. 2 shows the XRD patterns of the parent and recrystallized ferrierite materials. Although both show
18 diffraction peaks typical of highly crystalline ferrierite, the recrystallized material shows less intense
19 and broader peaks; reflecting a loss of crystallinity and the shortening of coherent diffraction domains
20 by the formation of mesopores [43] during recrystallization. No peaks are observed in the small angle
21 scattering region, indicating the absence of an ordered mesopore structure. On the other hand, no
22 other crystalline phase (SOD, GIS) or lamellar material was formed; such phases have been previously
23 reported when CTAB has not been used in the recrystallization [43].

24

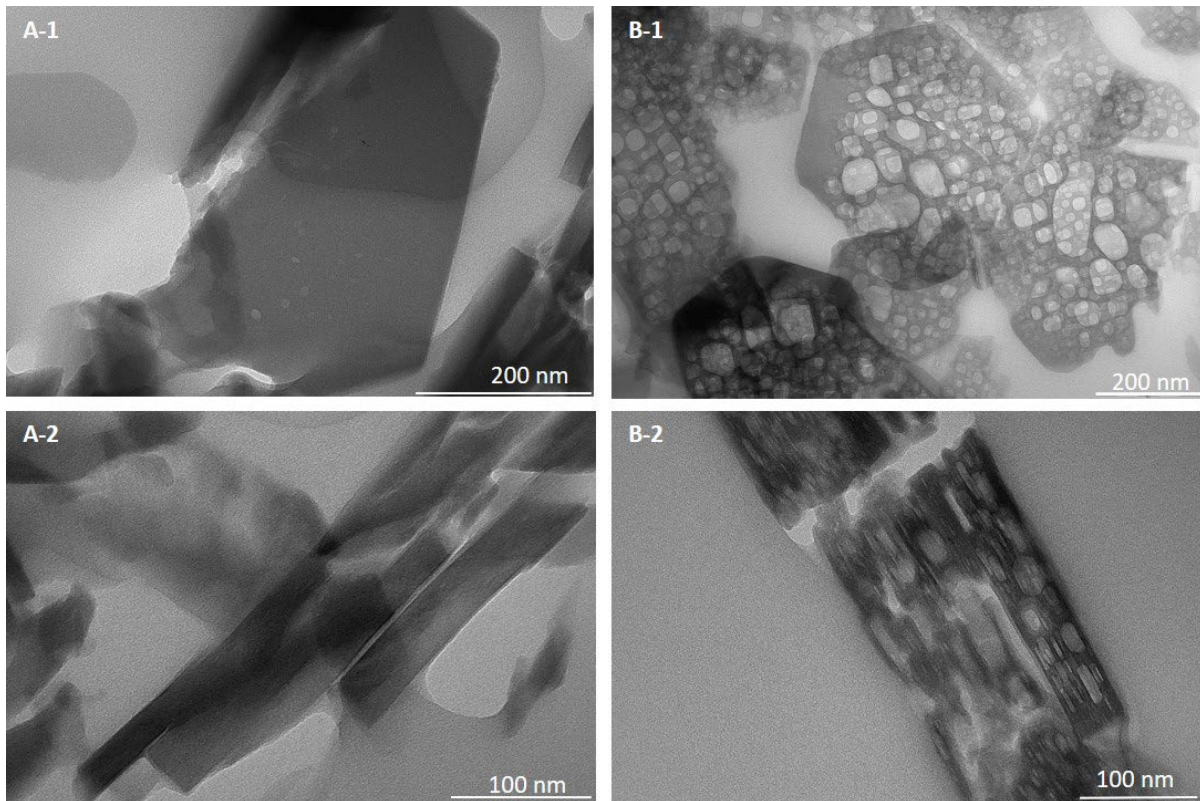
Table 1 Properties of the parent and recrystallized H-form-ferrierite materials.

Properties		H-FER-PE	H-FER-REC
Surface area (m^2/g)	S_{total}	379 \pm 24	406 \pm 15
	S_{micro}	340 \pm 24	248 \pm 14

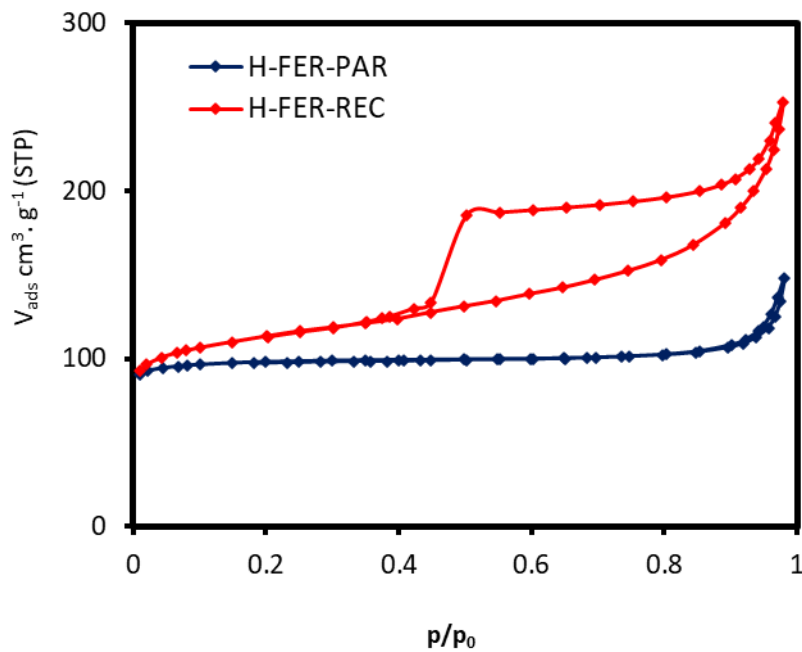
	S_{meso}	18 ± 2	76 ± 16
	S_{ext}	21 ± 7	82 ± 14
	V_{total}	0.20 ± 0.02	0.38 ± 0.03
Pore Volume (cm³/g)	V_{micro}	0.13 ± 0.01	0.10 ± 0.01
	V_{més0-intra}	0.01 ± 0.00	0.13 ± 0.02
	V_{meso-inter}	0.06 ± 0.02	0.15 ± 0.04
	Si/Al	9.7 ± 0.3	6.6 ± 0.3
	Total acidity (μmol/g STP)	1050 ± 31	720 ± 56

1

2 The transmission electron microscopy (TEM) micrographs of the H-form ferrierite-based zeolitic
3 materials along the [001] and [100] planes are shown in Fig. 3. On the one hand, the H-FER-PAR has
4 platelet-like crystals with very few small pores (Fig. 3-A1), which were not previously observed in
5 parent Na,K-Ferrierite [43], certainly due to the demetallation process occurring during ion exchange.
6 A slight increase in the Si/Al ratio from 9.2 in Na,K-FER to 9.7 in H-FER-PAR confirmed this (see Table
7 1). On the other hand, TEM images of H-FER-REC show a large number of parallelepiped mesopores
8 with blunt edges (Fig. 3-B1). There is a wide distribution of quasi-square mesopores with pore sizes
9 ranging from 10 to 50 nm in the [010] and [001] directions. Some larger pores are rectangular in shape
10 with length greater than 100 nm. They may be the result of merging of adjacent pores. According to
11 Fig. 3-B2, the mesopores have a thickness from 1.5 to 20 nm. Comparing Fig. 3-B1 and Fig. 3-B2, it can
12 be seen that the flat mesopores are parallel to the [100] platelet faces of the crystals and are located
13 in different layers from the surface to the interior of the crystals. TEM images allowing a statistics of
14 crystal size (see Fig S1) showed that the thickness of the FER crystals in the [100] direction appeared
15 to be smaller, less than 0.3 μm, in the recrystallized material than in the parent H-form material, where
16 more platelets with a thickness greater than 0.4 μm are observed. This suggests that the extension of
17 the flat mesopores can sometimes lead to a delamination of the ferrierite crystals.



1
2 **Fig. 3** TEM images of ferrierite materials (1) oriented on [100] (200 nm scale bars), and (2) oriented
3 on [010] (100 nm scale bars). A. Parent Ferrierite (H-FER-PAR). B. Recrystallized Ferrierite (H-FER-
4 REC).



5
6 **Fig. 4.** N₂ sorption isotherm curves of the H-form parent and recrystallized ferrierite-based materials.

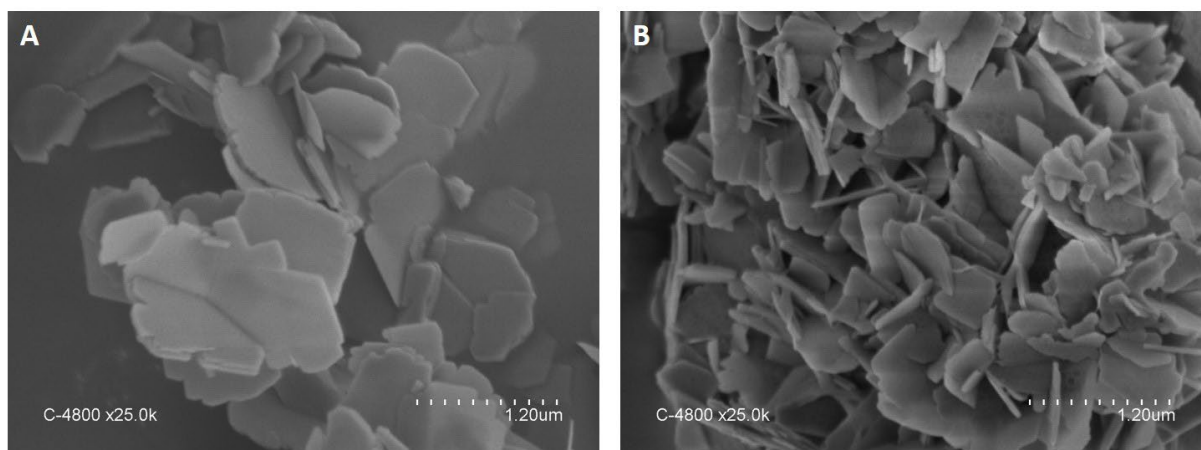


Fig. 5 SEM images of ferrierite materials with 1.2 μm scale bars. A. Parent Ferrierite (H-FER-PAR). B. Recrystallized Ferrierite (H-FER-REC).

According to the information summarized in Table 1, an increase in the volume of intracrystalline mesopores from 0.01 in H-FER-PAR to 0.13 cm^3/g in the recrystallized material, as well as in the volume of intercrystalline mesopores from 0.06 to 0.11 cm^3/g , confirms the presence of a new system of mesopores. The surface area of the mesopores increased from 18 to 76 m^2/g . The presence of a large hysteresis loop in the N_2 sorption isotherms of H-FER-REC (see Fig. 4), in contrast to the isotherms of the parent FER, confirms the presence of large mesopores, as previously reported by Cheng et al. [43]. The sharp desorption by cavitation at p/p^0 0.45 indicates that the mesopores are connected to the outer surface of the crystals by openings smaller than 4 nm, quite likely the structural microporosity of the zeolite. Although the surface area increased only slightly from 379 to 406 m^2/g , and the micropore volume decreased slightly from 0.13 to 0.10 cm^3/g , the outer surface area increased significantly from 21 to 82 m^2/g . This is consistent with the smaller size of the recrystallized ferrierite crystals compared to that of the parent ferrierite, as observed in the SEM images (Fig. 5) and also clearly seen in the TEM images (Fig S1).

On the other hand, the Si/Al ratio decreased significantly from 9.7 to 6.6 in the parent and recrystallized samples, respectively, due to the desilication process promoted by the base attack. Considering this change in Si/Al ratio, it may indicate that the recrystallization mechanism does not correspond to the mechanism proposed by Ivanova et al. [45] for two-step recrystallization, where the Si/Al ratio does not change during recrystallization. On the other hand, the behavior of this one-step recrystallization can be better explained by the crystal rearrangement mechanism proposed by García-Martínez and coworkers. [46]. As observed by ammonia temperature programmed desorption (TPD- NH_3) analysis (Fig S2), the most important change from H-FER-PAR to H-FER-REC was the decrease of the peak corresponding to the strong acidity. Minor changes were observed in the maximum peak temperature and total area related to the total acidity of the samples. The significantly higher amount of aluminum in the recrystallized ferrierite did not lead to an increase in acidity. In fact, the total acidity decreased from 1050 $\mu\text{mol}/\text{g}$ in H-FER-PAR to 720 $\mu\text{mol}/\text{g}$ in H-FER-REC with a larger proportion of the strongest acidic sites. This may be related to the partial destruction of the microporous crystal structure during the desilication process [47].

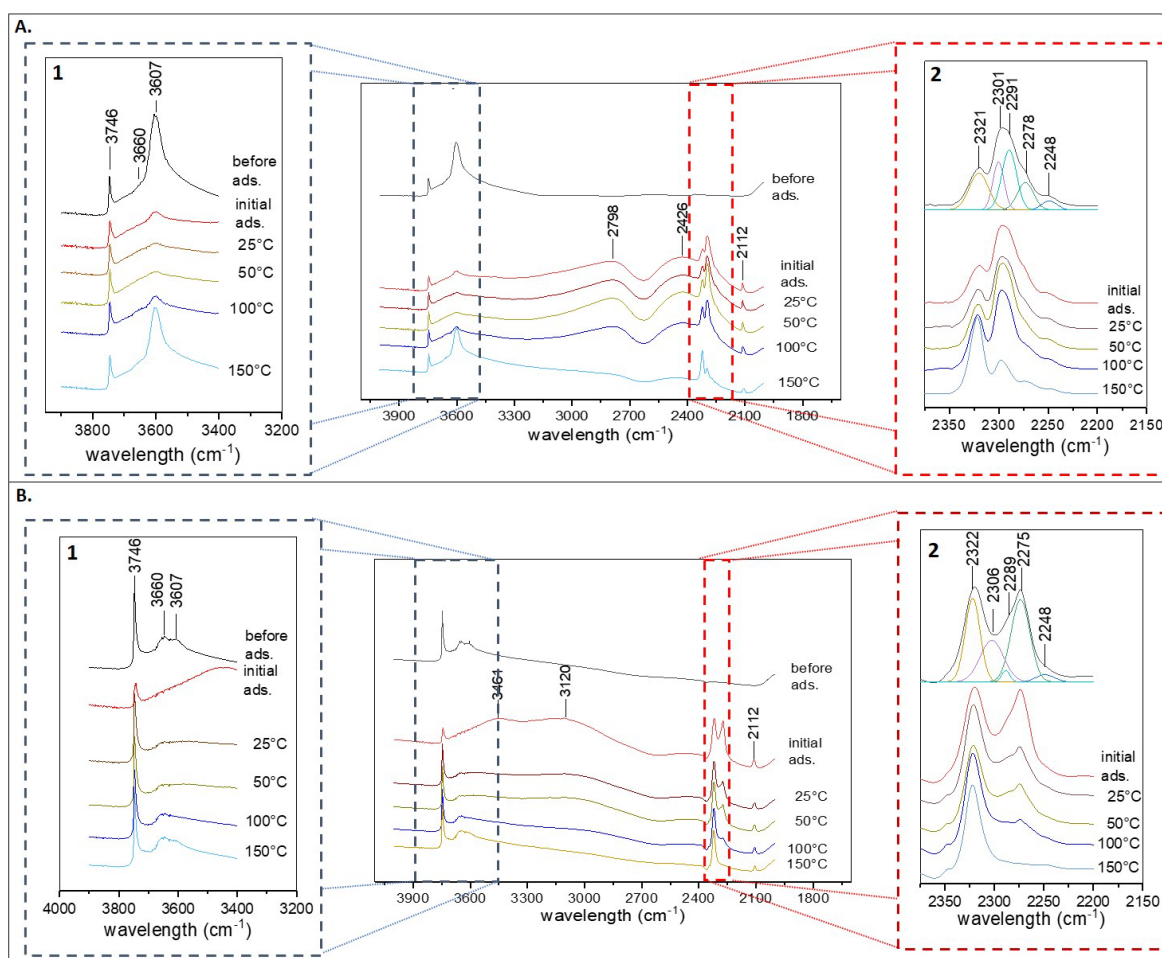
To confirm this solid-state NMR analyses of silicon and aluminum nuclei were performed on H-FER-PAR and H-FER-REC zeolitic materials.

1 On the one hand, by comparing the ^{27}Al MAS NMR spectra of the parent and recrystallized ferrierite
2 (Fig S3), the following differences were observed: the region of the signal around 0 ppm associated
3 with octahedral extra-framework aluminum (EFAL) species was increased from H-FER-PAR to H-FER-
4 REC. In addition, the area of the signal around 55 ppm decreased between H-FER-PAR and H-FER-REC,
5 indicating a smaller amount of tetrahedral aluminum species as part of the microporous crystalline
6 network of the zeolite. The width of the tetrahedral Al signal increased revealing an increase in disorder
7 in the zeolite phase as a result of a distribution of chemical environments and/or distances. As
8 expected, the amount of tetrahedral aluminum lost during recrystallization was proportional to the
9 loss of acidity. In addition, the appearance of a small peak around 30 ppm showed the presence of
10 pentahedral aluminum species associated with defects in the crystalline network of ferrierite.

11 By comparing the ^{29}Si MAS NMR spectra of the parent and recrystallized ferrierite (Fig S4), it was
12 possible to see that the amount of Si sites of Q_4 type, i.e. having only Si atoms in the second
13 coordination sphere (chemical shift (δ) at -116 ppm), does not change significantly between H-FER-
14 PAR (22.2%) and H-FER-REC (23.0%) materials. However, the amount of Q_4 -type Si atoms attached to
15 an Al atom (δ at -111 and -106 ppm) decreased from 75.6% in H-FER-PAR to 60.7% in H-FER-REC. This
16 clearly indicates that, despite the decreased Si/Al ratio in the solids, the fraction of Al in isostructural
17 substitution in the zeolite network has decreased. This is consistent with the observation of Al in extra-
18 framework octahedral species. The amount of Si sites with a chemical environment whose NMR
19 signature appears below -106 ppm (δ at -102 and -101 ppm) increased from 2.2% in H-FER-PAR to
20 16.4% in H-FER-REC. These signals could be associated with Q_3 Si sites, i.e. Si atoms with an OH group
21 in the coordination sphere. These Q_3 Si sites could be related to the formation of structural defects in
22 the zeolite corresponding to the extraction of aluminum or an amorphous aluminosilicate phase in the
23 sample.

24 In conclusion, the ^{27}Al and ^{29}Si NMR experiments revealed the presence of an Al-poor ferrierite phase
25 in H-FER-REC coexisting with extra-framework Al-rich species. In addition, the chemical environments
26 of Si and Al(IV) sites in the FER phase appear to be less ordered, as indicated by the increase in the
27 linewidths.

28 To better understand the changes in acidity properties upon recrystallization, infrared analysis of
29 adsorbed deuterated acetonitrile was performed on each of these materials. The use of CD_3CN , a weak
30 base, as a surface acidity probe appears to be relevant for identifying Lewis and Brønsted acid sites
31 and for differentiating and quantifying the strength of different Brønsted acid sites on the catalysts
32 [48]. Fig. 6 shows the FTIR spectra of parent and recrystallized ferrierite samples before and after
33 CD_3CN adsorption and at different temperatures during the desorption process.



1
 2 **Fig. 6** FTIR spectra of CD₃CN adsorbed on ferrierite as a function of desorption temperature of (A) H-
 3 FER-PAR and (B) H-FER-REC with the enlargement of the 3400-3900 cm⁻¹ zone (1) and the 2200-2400
 4 cm⁻¹ region with a model of the deconvolution procedure at initial CD₃CN adsorption (2)

5 The FTIR spectra of the parent and recrystallized significantly differ in the intensity of the OH stretching
 6 bands. The first band at 3746 cm⁻¹ can be assigned to the ν(OH) of the terminal silanol groups (Si-OH)
 7 [44,49,50]. The band at 3741 cm⁻¹ is more intense in H-FER-REC, indicating a greater amount of
 8 terminal silanols in this material. It is expected that the silanol groups are formed during the opening
 9 of structural defects or the formation of an amorphous phase upon recrystallization. This band is
 10 consistent with the observation of more Si Q₃ sites in H-FER-REC. The band at 3660 cm⁻¹ can be
 11 attributed to ν(OH) present in extra-framework species, it is often associated in the literature with a
 12 band at 3780 cm⁻¹, characteristic of acidic OH groups bound to extra-framework aluminum, which is
 13 not observed in the present spectra [44]. The last band present in both spectra at 3607 cm⁻¹
 14 corresponds to the bridged hydroxyl groups (Si-OH-Al) on the ferrierite structure [49–51]. The band at
 15 3607 cm⁻¹ is broad and asymmetric because several types of bridging hydroxyls are present in different
 16 environments, as already shown by several studies [51,52]. The intensity of the band assigned to
 17 bridging hydroxyl groups (Si-OH-Al) is significantly lower in the recrystallized sample, which is certainly
 18 due to the loss of part of the microporous crystal framework of ferrierite during recrystallization. This
 19 is consistent with the lower amount of Q₄(1Al) silicon sites observed by ²⁹Si NMR.

20 The adsorption of CD₃CN led to a significant decrease of the terminal silanol band at 3741 cm⁻¹ and to
 21 the near disappearance of the bands from 3730 to 3550 cm⁻¹ corresponding to bridged hydroxyls in

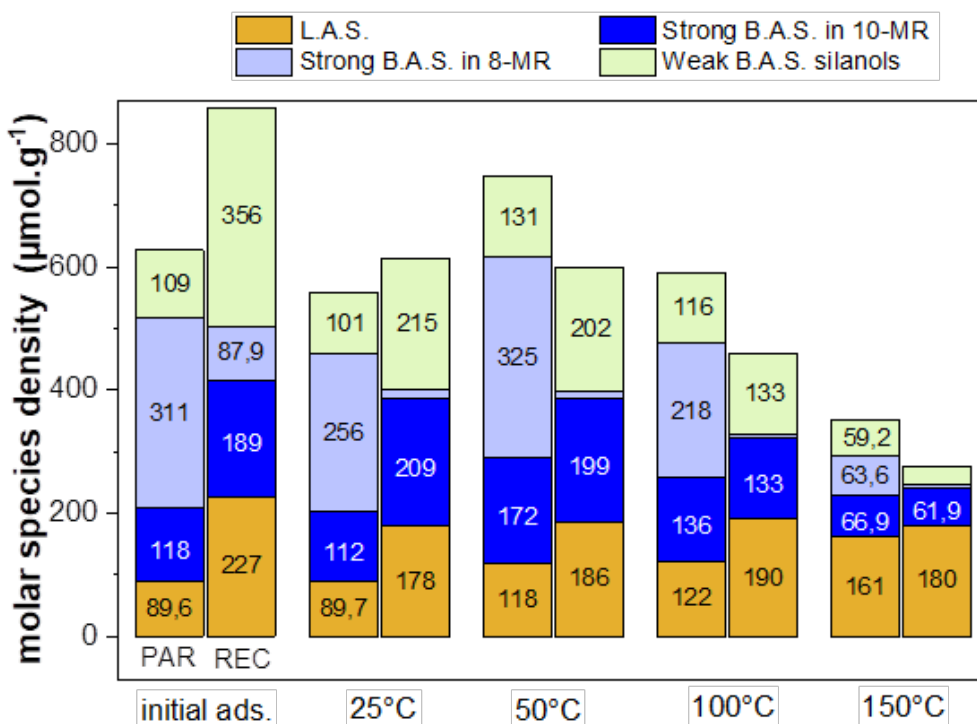
1 both samples (see Fig. 6). The disappearance of the bridged hydroxyl bands in H-FER-PAR is
2 accompanied by the development of broad bands centered at 2798 and 2425 cm^{-1} , corresponding to
3 Fermi resonances between the modes of vibration of the adduct of CD_3CN with strong Brönsted sites
4 [53,54]. In the case of H-FER-REC, the decrease of the 3746 cm^{-1} signal with adsorption is accompanied
5 by the formation of broad bands at 3464 and 3120 cm^{-1} , the first one typical of the interaction of CD_3CN
6 with silanols and the second one generally observed on amorphous silica-alumina, also derived from
7 amorphisation of zeolites [54-57].

8 With CD_3CN adsorption, two broad bands appeared between 2400 and 2200 cm^{-1} , corresponding to
9 the acetonitrile bands in OH-NCCD₃ molecular complexes between the bridged hydroxyl groups and
10 the acetonitrile on the surface. These bands are typical of strong acid sites on the surface [49]. An
11 enlargement of this region is shown in Fig. 6 for both materials. Two weak bands at 2112 and 2248 cm^{-1} ,
12 which are present throughout the CD_3CN adsorption process and are not modified by the desorption
13 process, can be assigned to the frequencies $\nu_s(\text{CD}_3)$ and $\nu_{as}(\text{CD}_3)$. In the $\nu(\text{CN})$ spectral region, the two
14 broad bands obtained, the first from 2350 to 2310 cm^{-1} and the second from 2310 to 2250 cm^{-1} , were
15 assigned to Lewis and Brönsted acidic sites, based on data found in the literature [44,49,54,58,59].
16 These bands are composites with several components identified in both materials after deconvolution
17 of the spectra. The band at 2278 cm^{-1} on H-FER-PAR and 2275 cm^{-1} on H-FER-REC corresponds to
18 adsorption on silanols, which are weak Brönsted acids, in agreement with previous studies in the
19 literature [54,60]. The band at 2291 cm^{-1} on H-FER-PAR and 2289 cm^{-1} on H-FER-REC and the band at
20 2301 cm^{-1} on H-FER-PAR and 2306 cm^{-1} on H-FER-REC are attributed to the adsorption of CD_3CN
21 adducts with acidic sites on the bridged hydroxyl groups present in the 8-MR (8-member ring) and 10-
22 MR channels, corresponding to strong Brönsted acid sites. The band at 2321 cm^{-1} on H-FER-PAR and
23 2322 cm^{-1} on H-FER-REC corresponds to acetonitrile adsorbed on Lewis acidic sites [44,49,54,58,59].
24 The presence of Lewis sites is frequent in ferrierite, a zeolite easily subject to dehydroxylation of
25 Brönsted sites [61]. Comparing H-FER-PAR and H-FER-REC in the CN spectral region (Fig. 6 A and Fig. 6
26 B) after desorption at 25°C, it can be seen that the ratio of Brönsted to Lewis acid sites decreases upon
27 recrystallization; this is both a consequence of the decrease in the amount of strong Brönsted sites and
28 the increase of the Lewis site. The formation of Lewis acid-active EFALs would be itself related to the
29 increase in terminal silanols in H-FER-REC.

30 It has been observed that, in the comparison of different zeolites, the highest acid strength
31 corresponded to the highest wavenumber of CD_3CN adsorbed on Brönsted sites [48,53,62].
32 Considering that the most stable Brönsted sites of ferrierite are located in the [8²6²6⁴5⁸] cavity
33 between two 8-MRs [63], the deconvoluted band at 2291 cm^{-1} in H-FER-PAR and 2289 cm^{-1} in H-FER-
34 REC was assigned to the acidic sites within the 8-MR channels while the band at 2301 cm^{-1} in H-FER-
35 PAR and 2306 cm^{-1} in H-FER-REC was assigned to the acidic sites within the 10-MR channels. An
36 interesting feature is that the relative content of the Brönsted acid sites in 8-MR decreases significantly
37 upon recrystallization, compared to the sites in 10-MR environments. This could be related to already
38 observed effects of recrystallization, namely the increase of silanols and Lewis sites. A local
39 accumulation of EFAL species in the most constrained 8-MR channels would prevent the accessibility
40 of strong Brönsted sites in the [8²6²6⁴5⁸] cavity.

41 Let us study the evolution of the signals as a function of the temperature of acetonitrile desorption. In
42 the parent and recrystallized FER materials, the relative intensity of CN vibrations corresponding to
43 bridged silanols (considering OH together in 8-MR and 10-MR) decreases less rapidly as a function of

1 desorption temperature than the signal associated with terminal silanols. This is consistent with the
 2 higher acid strength of bridging silanols in Si-OH-Al groups.



3
 4 **Fig. 7** Comparison of the molar density of acidic sites between parent (H-FER-PAR) and recrystallized
 5 (H-FER-REC) catalytic materials.

6 The band deconvolution allowed us to calculate the molar density of the acid sites and thus to compare
 7 their evolution with the desorption temperature and between the two samples (Fig. 7). A larger
 8 number of total acid sites was reported on the surface of the recrystallized ferrierite immediately after
 9 adsorption of CD₃CN, mainly due to a larger amount of physisorbed CD₃CN on silanols, the weak
 10 Brönsted acid sites, at 2278 cm⁻¹. This was clearly a result of the formation of amorphous silica or
 11 defects in the zeolite framework with the desilication treatment, which also accounted for the increase
 12 of Lewis acid EFAL in H-FER-REC. Considering the reported extinction coefficients for each type of acid
 13 site, the molar density for each site was calculated. Although there is a higher amount of weak
 14 Brönsted acid sites (silanols) in H-FER-REC (215 μmol/g) than in H-FER-PAR (101 μmol/g) at 25°C, the
 15 ratio between them decreases significantly with desorption, indicating a very weak adsorption on the
 16 desilication-issued silanols. It is also interesting to note that the sum of Lewis and Brönsted acid sites
 17 originating from Al atoms is proportional to the variation of the Si/Al ratio in these ferrierite-based
 18 materials (H-FER-PAR: 458 μmol/g, H-FER-REC: 400 μmol/g). However, with recrystallization the
 19 number of strong Brönsted sites in 8MR decreased and virtually disappeared at higher temperature,
 20 while there was a significant increase in the amount of Brönsted acid sites from bridged hydroxyl
 21 groups in 10-MR. Preferential dealumination in 8-MR cavities and in-situ deposition of EFAL could
 22 explain both phenomena. Indeed, it has been shown that protons are extremely mobile in H-ferrierite
 23 and their location on oxygen atoms connected to Al atoms of the network is strongly dependent on
 24 the interaction with adsorbed molecules [64]. The protons of acid sites related to Al₂ and Al₄ sites, at
 25 the rim between 8-MR and 10-MR, if no more accessible through 8-MR could be reoriented on a
 26 neighbor oxygen and interact with CD₃CN molecules in the 10-MR.

1 Furthermore, as the desorption temperature was increased, the number of adsorbed CD₃CN molecules
2 was found to be lower. This is related to its desorption from weaker acidic sites. At the highest
3 temperature studied, 150°C, it is noteworthy that the molar density of adsorbed molecules on Lewis
4 acid sites is approximately similar for both materials. In contrast, the number of molecules adsorbed
5 on Brönsted acid sites decreased with temperature. At 150°C, it was observed that the CD₃CN
6 molecules adsorbed on Brönsted acid sites were higher in the H-FER-PAR (131 µmol/g) than in the H-
7 FER-REC (65 µmol/g) and no adsorption took place on 8-MR Brönsted sites. This allowed us to confirm
8 the loss of Brönsted acid sites during the recrystallization process.

9 In conclusion, from the characterization of the zeolitic material obtained by one-step recrystallization
10 of low silica ferrierite, we observe the formation of a microporous ferrierite structure with embedded
11 mesopores. In agreement with the results obtained by Cheng *et al.*[43], this mesopore system is
12 composed of parallelepiped mesopores with sizes ranging from 10 to 50 nm, which are connected to
13 the outer surface by micropores. A loss of about a quarter of the micropore volume and about a third
14 of the total acidity of the parent material is observed. This may be related to the dissolution of part of
15 the ferrierite crystalline structure. Furthermore, the loss of acidity was directly proportional to the loss
16 of tetrahedral aluminum species corresponding to the Brönsted acid sites of the ferrierite structure. In
17 addition, the presence of a higher amount of weaker Brönsted acid sites associated with terminal
18 silanols in H-FER-REC is certainly associated with the growth of a mesoporous phase on the zeolite
19 crystals. This new weak Brönsted acidity is certainly not strong enough to participate in reactions
20 requiring strong acid sites, so the new mesoporous system may simply increase the accessibility to
21 other efficient Brönsted acid sites.

22 In previous studies, a secondary ordered mesoporous system or meso-microporous materials have
23 been obtained in various ways (pillaring [65,66], transformation of larger-porosity zeolites [37],
24 simultaneous synthesis of meso and microporous phases [67,68], synthesis of nano-stacked ferrierite
25 crystals [69], or recrystallization processes on commercial zeolitic phases [43,70,71]) have been shown
26 to improve diffusion, increase acid sites accessibility, and decrease catalyst deactivation rates in
27 reactions such as 1-butene skeletal or oleic acid isomerization [37,70,72].

28

29 **3.2 Catalytic Tests**

30 The recrystallized ferrierite and its parent material have been evaluated as catalysts in methyl oleate
31 isomerization in batch and continuous flow reactors. Various parameters such as activity, conversion,
32 selectivity, and deactivation were evaluated.

33 The isomerization reaction of methyl oleate using these materials resulted in a mixture of products in
34 the gas and liquid phases with high complexity. Different types of products are obtained due to the
35 different reactions occurring under the studied conditions, such as isomerization, cracking, and
36 oligomerization (Fig S5).

37 On the one hand, the different products present in the liquid phase were analyzed by gas
38 chromatography. A typical liquid phase chromatogram shows the presence of monomers and
39 oligomers (see Fig S6).

1 Further analysis of the monomer fraction revealed five types of compounds (see Fig S7). First, a large
 2 number of linear C₁₈ mono-unsaturated fatty acid methyl esters were detected (Fig S7-i.). These types
 3 of compounds have been observed previously by Ngo et al. [73] but were not quantified as products
 4 but as intermediates [73,74]. Their identification and characterization is essential, as the position or
 5 geometry of the double bond in the methyl ester can affect their properties and applications [75]. The
 6 second group, the target of our synthesis (Fig S7-ii.) corresponds to the branched-chain C₁₈ fatty acid
 7 methyl esters that result from the skeletal rearrangement of the positional and geometrical isomers
 8 of methyl oleate. The third compound observed is methyl stearate (Fig S7-iii). The fourth group (Fig S7-
 9 iv.) corresponds to lactones and the fifth group (Fig S7-v) corresponds to cracking products such as
 10 some unsaturated hydrocarbons and shorter fatty acid methyl esters that remain in the liquid fraction.

11 In addition, analysis of the liquid phase by MALDI-TOF (mass spectra in Fig S8) showed in addition to
 12 the previously described products, there were products corresponding to oligomers with molecular
 13 weights of 530 to 600 g/mol. Further MS-MS analysis was performed on the most intense M/Z peaks,
 14 585.5 and 599.6 (Fig S9). The peak of M/Z=585.5 broke down mainly into an ion fragment with M/Z of
 15 303.3, representing the monomer of oleic acid, it could be assigned to dimer estolides. Then, the peak
 16 at M/Z=585.5, which is fragmented into peaks with M/Z different from 303.3, could be assigned to the
 17 dimers of oleic acid.

18 On the other hand, GC analysis of the gas phase showed the presence of several cracking products and
 19 their derivatives. Carbon dioxide, water and methanol were also observed, as well as considerable
 20 amounts of dimethyl ether, short hydrocarbons and their isomers with carbon chain lengths ranging
 21 from three to seven carbons. These hydrocarbons are predominantly branched and unsaturated (Fig
 22 S10).

23

24 3.2.1 Methyl oleate isomerization in a batch reactor.

25 The first methyl oleate isomerization experiments were carried out in a batch reactor to evaluate the
 26 potential of the recrystallized ferrierite in this reaction and also to adjust the best possible reaction
 27 conditions. The first tests were carried out according to the best conditions reported in the literature
 28 for the production of isostearic acid from oleic acid, i.e. temperatures between 260°C and 285°C,
 29 pressures between 2 and 4 MPa and a catalyst amount of 5 wt% [15]. The results of methyl oleate
 30 isomerization are summarized in Table 2.

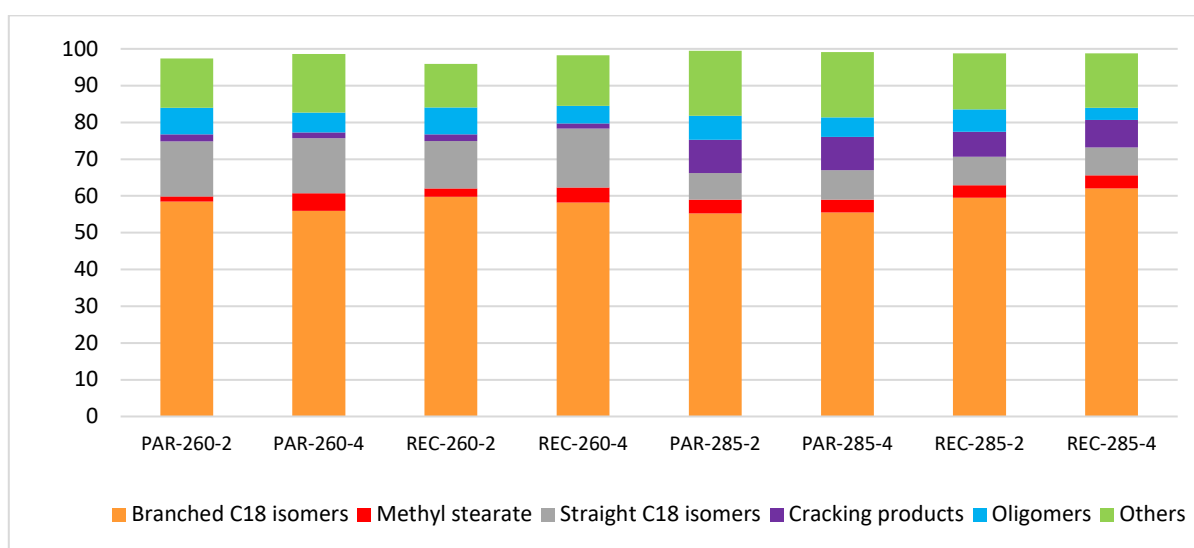
31 **Table 2** Methyl oleate isomerization conversion, selectivity, and yield in branched product values
 32 (Cat. amount: 5 wt %; reaction time: 8h; N₂ atmosphere; batch reactor).

Temp (°C)	Catalyst	Pressure (Mpa)	Conversion (%)	Branched-chain C ₁₈ products		Coke amount in spent catalyst ^a (% wt.)
				Selectivity (%)	Yield (%)	
260	H-FER-PAR	2.0	97.4	60.0	58.4	14.5
		4.0	98.6	56.7	55.9	11.6
	H-FER-REC	2.0	95.9	62.3	59.8	19.3
		4.0	98.3	59.2	58.2	20.3
285	H-FER-PAR	2.0	99.4	55.6	55.3	13.5
		4.0	99.1	56.0	55.5	13.4
	H-FER-REC	2.0	98.8	60.2	59.5	17.9

	4.0	98.7	62.8	62.0	18.9
--	-----	------	------	------	------

^a Calculated from TGA results as the sum of mass losses from 250 to 700°C

1
2 The yields in branched chain products obtained for the methyl oleate isomerization in this work under
3 batch conditions were better than previously reported values. Fig. 8 shows the conversion and yield
4 obtained in the methyl oleate isomerization under batch conditions. The best yield value for C₁₈
5 branched chain products, 62.8%, was found using the recrystallized ferrierite as catalyst at 285°C.
6 Yields were greater than 55% in all tests. The use of ferrierite as a catalyst in this reaction was
7 previously described. It was concluded that a ferrierite with a low Si/Al ratio and few high strength
8 Brönsted acid sites in the 10-membered rings (10-MR) promotes the yields to branched products [74].
9 Although it has been described that the use of ferrierite together with some additives such as water
10 and bulky hindered Lewis base molecules led these yields to reach values up to 80% [25,30,36,76,77],
11 yields above 42% had not been obtained in the methyl oleate isomerization reaction [25].



12
13 **Fig. 8** Methyl oleate isomerization products yields obtained using H-FER-PAR and H-FER-REC as
14 catalysts at different temperatures (260, 285°C) and pressures (2.0, 4.0 MPa) in batch reactor for 8 h.

15 In all our tests, the use of recrystallized ferrierite -H-FER-REC- showed a better yield of branched
16 isomers compared to the parent exchanged ferrierite -H-FER-PAR. The use of H-FER-REC also brought
17 to a slight decrease of conversion, a decrease of measured oligomerisation products and an increase
18 of coke formation. The increase of temperature from 260 to 285 °C led to a systematic increase of
19 conversion, decreasing of oligomerisation products and formation of more cracking products. At the
20 highest temperature, the yield of branched products generally decreased, except when H-FER-REC was
21 used at high N₂ pressure. The pressure of the inert gas has been generally considered having a limited
22 influence on isomerization, albeit a slight increase of branched isomers with pressure has been
23 observed on ferrierite and zeolite beta [23,78].

24 The observed effects could be mainly related to the recrystallization-induced changes in number and
25 distribution of acid sites (Fig. 7). The effect of the greater accessibility to the micropore network on H-
26 FER-REC compared to H-FER-PAR has also to be considered. This could lead to higher yields of branched
27 products according to the pore mouth hypothesis [70,74]. Wiedemann *et al.* found that pore blockage
28 occurs at a very early stage. It starts with the intermolecular H-transfer reactions that lead to the

1 appearance of unsaturated carbocations, followed by the formation of cyclic conjugated ketones as
2 precursors of alkyl benzenes [25]. It leads to the formation of highly carbonaceous materials that block
3 the channels. As previously described for ferrierite, this first channel blockage [79] allows catalytic
4 activity only in the acidic sites of the pore mouth of the 10-membered ring (10-MR) channels [74],
5 which represents less than 20% of the total Brönsted acid sites in unmodified ferrierite [51]. Although
6 the recrystallized materials have fewer strong Brönsted acid sites, as shown by FT-IR spectroscopy
7 using acetonitrile as a probe, they present more strong Brönsted sites in 10-MR than the parent zeolite
8 (Fig. 7). Moreover, the formation of mesopores in the recrystallization has shortened the length of the
9 [010] 10-MR pores and led to a four-fold increase in the mesopore surface (Tab. 1), allowing an
10 excellent access to the new pore mouths where the active sites are located, improving the interaction
11 between the substrate and the internal acid sites. Although the recrystallized material -H-FER-REC- has
12 higher amounts of other acidic sites, the weakest Brönsted acidic sites of silanols are not strong enough
13 to participate in the isomerization reaction and also Lewis acid sites on zeolites are considered inactive
14 in olefin oligomerisation [80]. According to Wiedemann *et al.*, just the Brönsted acidic sites of high
15 strength on the pore mouth of the 10-MR channels can carry out this reaction [74].

16 It can be argued if a higher diffusivity of the coke precursors due to the presence of mesopores can
17 also play a role, despite the special geometry of the constrained mesopores of ferrierite. This could
18 delay the deactivation of the acidic sites, allowing them to convert more molecules. It has been
19 reported previously [41,81,82] that the formation of a mesoporous network, especially when
20 hierarchically organized with micropores, can improve selectivity by shortening the diffusion path and
21 avoiding secondary reactions. Although the yields of branched chain products have been improved
22 over the commercial process using montmorillonite clay and a regeneration method has been
23 developed [83], a fast deactivation caused by pore blockage is the main reason why this process is less
24 economically competitive than the commercial oleic acid dimerization process [25]. Furthermore,
25 acidic site poisoning also occurred during the isomerization reaction by strong adsorption of polyenylic
26 species. This leads to deactivation processes of active sites at the pore mouths. Under these conditions,
27 catalyst particles are underutilized [84], reaction rates are lower [85,86], and this coke formation
28 [27,12] leads to faster deactivation of catalysts [87].

29 To gain insight into catalyst deactivation and the nature of the deactivation-causing coke, the spent
30 catalyst materials were washed and the liquid extracts were analyzed by GC-MS and MALDI-TOF. The
31 solid portion of the spent catalyst was analyzed by TGA to assess the amount of coke remaining on the
32 ferrierite, and ¹³C CP MAS NMR analysis was performed to provide insight into the nature of the
33 carbonaceous material present on the spent catalysts. The spent materials were first washed with
34 acetone to remove residual reaction products and reactants, following the work of Wiedemann [87].
35 This was followed by a 24 h Soxhlet extraction with dichloromethane. This procedure removed soluble
36 coke components that were not within the pore network of the spent catalyst [88,89]. GC-MS and
37 MALDI-TOF analysis of the extracted liquid phase after the first acetone wash showed that only traces
38 of reaction products remained that were not removed after filtration. Typical MALDI-TOF spectra
39 obtained from the liquid phase extracted with dichloromethane in the second step are shown in Fig
40 S11. Although they showed minimal remnants of methyl oleate isomerization reaction products, the
41 main peak obtained in all spectra of the MALDI-TOF analysis is related to alkylbenzene production
42 intermediates ($[C_{19}H_{33}O]^+=277$) previously observed in the literature as coke precursors [5,25]. This
43 precursor was identified by MS-MS analysis at $m/z=277$ corresponding to 1-dodecyl-6-
44 methoxycyclohexa-1,3-diene. Methyl losses were detected in the mass spectrum corresponding to the

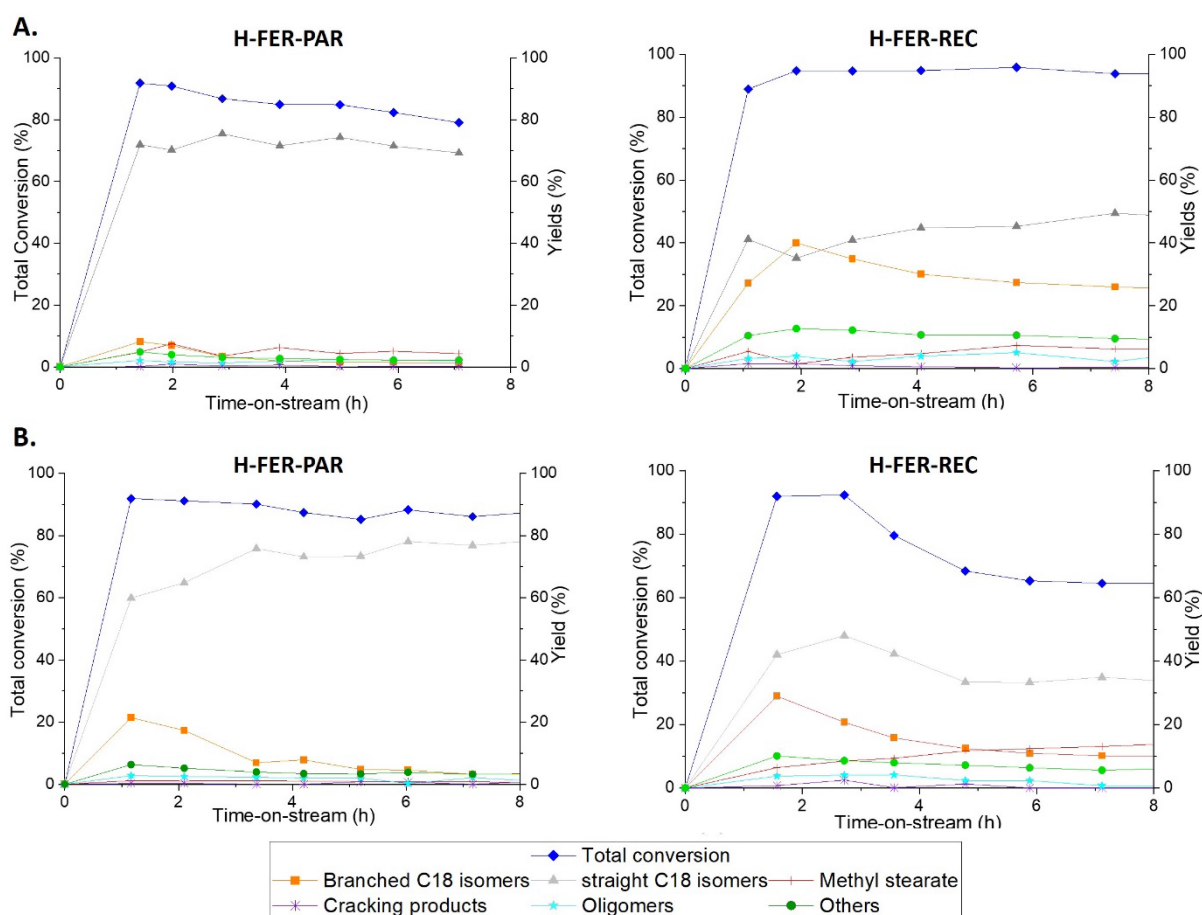
1 peaks at m/z 269 ($[\text{C}_{18}\text{H}_{30}\text{O}]\text{Li}^+$) and at $m/z=262$ ($[\text{C}_{18}\text{H}_{30}\text{O}]^+$). The peak at $m/z=183$ of formula
2 $[\text{C}_{12}\text{H}_{15}\text{O}]\text{Li}^+$ corresponds to the loss of hexane, while the peak at $m/z=121$ corresponds to the formula
3 $[\text{C}_8\text{H}_9\text{O}]^+$, the peak at $m/z=108$ corresponds to methoxyphenyl $[\text{C}_7\text{H}_8\text{O}]^+$ and the fragment at $m/z=77$ is
4 the phenyl $[\text{C}_6\text{H}_5]^+$ radical, allowing us to conclude the presence of aromatic compounds in this extract.

5 Thermogravimetric analysis (TGA) results of the spent catalyst (Fig S12) showed three stages of mass
6 loss previously associated with residual traces of highly volatile products (120-250°C), residual high
7 molecular weight products, non-polyaromatic (250-400°C), and polyaromatic coke (400-700°C). The
8 amount of coke in the spent catalyst was calculated from the TGA results as the sum of the mass losses
9 from 250 to 700°C and the results are shown in Table 2. A higher amount of organic residues was
10 observed in the spent catalysts derived from the recrystallized ferrierite -H-FER-REC- than in the spent
11 catalyst derived from the parent exchanged ferrierite -H-FER-PAR-. This was observed at both
12 temperatures studied. These higher amounts of coke can be explained by the presence of mesopores
13 where more coke can be deposited. Although this new mesoporous network could enhance the
14 transport of coke precursors out of the micropore ferrierite structure, the fact that these mesopores
15 are connected to the outer surface of the crystals by micropores could prevent these precursors from
16 leaving the particles of the catalytic material. This is also consistent with the fact that these
17 experiments are performed in a batch reactor (without the possibility to follow the reaction kinetics
18 due to too many experimental hurdles), which means that the time when the maximum conversion is
19 reached is unknown. The remaining reaction time after the maximum conversion is reached can lead
20 to the formation of by-products and/or coke. This is likely to occur when the reactants can no longer
21 diffuse to catalytic sites and thus can no longer be converted within the zeolite channels due to the
22 selectivity created by the presence of the microporous channel.

23 To further analyze the coke, the ^{13}C CP MAS NMR spectrum of the spent catalyst was recorded to
24 provide insight into the nature of the carbonaceous material (see Fig S13). Overall, the signals from 0
25 to 70 ppm were assigned to aliphatic carbons, while the signal at about 130 ppm was assigned to
26 aromatic carbons [90-92]. Among the signals obtained between 0 and 70 ppm, the signals from 10 to
27 20 ppm were assigned to the methyl groups ($-\text{CH}_3$) of the aliphatic chains, while the signals from 20 to
28 35 ppm were assigned to the methylene groups ($-\text{CH}_2-$) of the aliphatic chains [82]. Another signal
29 around 60 ppm was assigned to the methylene groups in the alpha or beta position on a heteroatom
30 such as oxygen [90,92]. The primary signal of the latter group in the spent catalysts at 260°C (spectra i
31 and ii) could be closer to an aromatic ring, leading to a downfield shift in the spectrum. This could
32 indicate a higher aromaticity in this spent catalyst. The same phenomenon is observed in the spectra
33 of spent catalysts used in the reaction at 285°C (spectra iii and iv-S13). The signal present around 60
34 ppm, particularly intense in spectra iii-S13, indicates the presence of oxygen in the coke. The broad
35 peak around 130 ppm was assigned to the carbons of the aromatic rings. More intense signals assigned
36 to aromatic carbons can be observed in the spent catalysts of the tests at 285°C. This could be due to
37 greater aromatization at 285°C. This hypothesis is confirmed by the lower intensity in these spectra of
38 the signal around 60 ppm related to methylene close to oxygen in the experiments at 285°C compared
39 to those carried out at 260°C, indicating a lower amount of this element in the coke. Although the
40 nature of the coke was significantly affected by the conditions of pressure or temperature, a significant
41 difference was not observed as the coke present in the spent catalysts derived from H-FER-REC and H-
42 FER-PAR.

43 3.2.2 Methyl oleate isomerization in a continuous flow reactor.

1 It has to be observed that in the batch reactor, in the absence of kinetic monitoring, the time-
 2 dependent changes in conversion and selectivity cannot be determined. In order to better understand
 3 the catalytic performance of these materials for future industrial applications, and to complement the
 4 results already obtained in a batch reactor, the methyl oleate isomerization reaction was carried out
 5 in a continuous flow reactor with a fixed bed downstream. A very recent work on methyl oleate
 6 isomerization has been reported in flow reactor using different unmodified zeolites [93]. Long-term
 7 experiments were carried out at one temperature, 290°C, and the best performance was obtained with
 8 an H-mordenite catalyst (Si:Al ratio=20) for 48 h long tests. However, the effect introducing
 9 mesoporosity into the zeolite framework was not investigated. This type of reaction was carried out in
 10 a continuous flow reactor. These experiments allow us to evaluate the behavior and robustness of such
 11 catalytic systems. The reaction was carried out with H-FER-PAR and H-FER-REC, both at a weight hourly
 12 space velocity (W.H.S.V.) of 3.5 h⁻¹ at 260 and 285°C as well as pressures of 2.0 and 4.0 MPa, in order
 13 to have conditions comparable to those studied in batch.



14
 15 **Fig. 9.** Methyl oleate isomerization in a continuous flow reactor at 260°C and pressures of **A.** 2.0 MPa
 16 and **B.** 4.0 MPa, using ferrieritic materials as catalysts.

17 At 260°C and a pressure of 2.0 MPa (Fig. 9-A), the H-FER-PAR and H-FER-REC catalytic materials show
 18 similar conversion behavior, with a high and stable value over several hours and a high and fairly stable
 19 yield (with a slight increase in the case of recrystallized ferrierite) of straight C₁₈ double bond
 20 positional/geometric (cis/trans) isomers of methyl oleate with about 70% for the parent sample and
 21 about 40% for the recrystallized sample. These yield levels were not observed in the batch reactor.
 22 Regarding the yields of branched C₁₈ isomers, which are the desired products, under these pressure

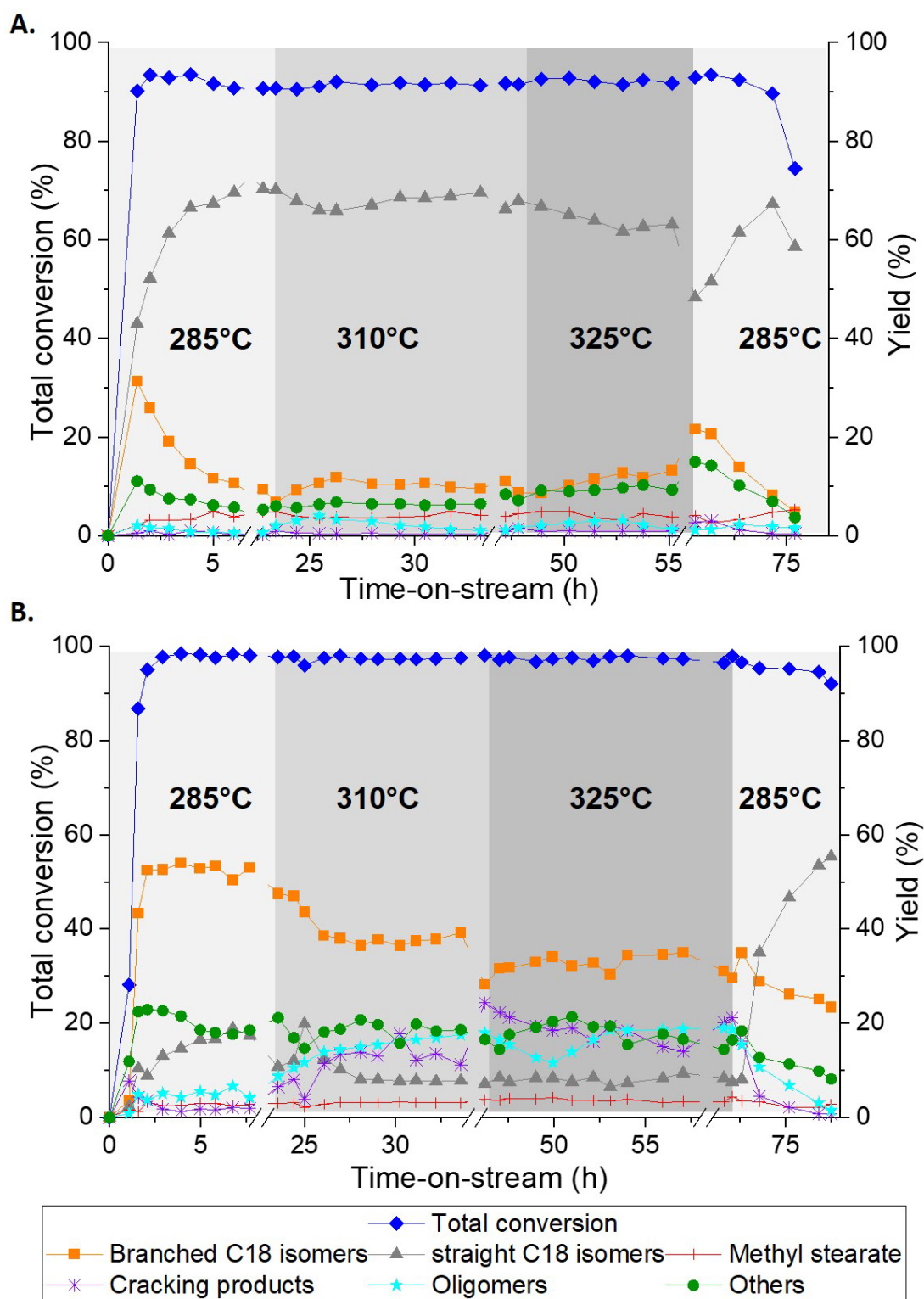
1 and temperature conditions, they were quite stable (H-FER-PAR Y_{bc} : 8.2%; H-FER-REC Y_{bc} : 40.0%) but
2 low compared to the results obtained in batch conditions (H-FER-PAR Y_{bc} : 58.4%; H-FER-REC Y_{bc} : 59.8%)
3 especially for the parent sample, for which the difference is huge. This behavior can be explained by a
4 shorter contact time between the catalytic material particles and the methyl oleate compared to the
5 batch reactor (8h of reaction), which is not sufficient to allow consecutive reactions, generally leading
6 to the formation of branched products. When comparing the yields of branched products using the
7 parent and recrystallized samples, the difference is striking (about 40% with a slow decrease with time
8 on stream for the recrystallized sample and about 8% for the parent sample), since they were almost
9 at the same level in the batch reactor. Indeed, as shown by the FT-IR results, H-FER-rec has a higher
10 amount of strong Brønsted acid sites in the 10-MR pores. Moreover, the contact between the methyl
11 oleate molecules and the acidic sites present at the mouth of the 10-MR channels is favored by the
12 high area at the surface of mesopores. Looking specifically at the results obtained with H-FER-PAR, the
13 yields of branched chain products (8.2%) and other by-products were low. Using the parent ferrierite
14 sample, the maximum yield (10%) was reached after one hour of time on stream and its value
15 decreased rapidly, probably due to the deactivation of the few strong Brønsted acid sites located in
16 the pore mouths. In contrast, using recrystallized ferrierite as a catalyst, the maximum yield of
17 branched products (42.5%) was reached after 2h of time on stream, and its value slowly decreased to
18 30%. This may be due to the new mesoporous system, which can slow down the pore blocking
19 phenomenon by allowing the precursors of coke formation to spread from the micropore system into
20 the mesopores. Considering that these mesopores are connected to the outer surface by micropores,
21 when these precursors grow by oligomerization reaction, they could not leave the ferrierite particles,
22 thus delaying the deactivation phenomena. This is confirmed by the increase in the production of by-
23 products such as methyl stearate, lactones and oligomers, which started to increase simultaneously
24 with the decrease in the production of branched products. At this point, due to the blockage of the
25 internal acid sites, the catalytic activity of the external acid sites was greater, resulting in a loss of
26 selectivity.

27 Looking more broadly at catalyst deactivation, shorter contact times in a flow reactor are beneficial for
28 catalyst behavior, as conversions slowly decrease during the first few hours of reaction and then
29 remain remarkably stable with time on stream. This is further supported by the amount of oligomers
30 under continuous flow conditions, which decreases dramatically for both catalysts compared to batch
31 conditions. Under these flow conditions, the short contact times probably lead to a lower probability
32 of molecules being adsorbed on the external acidic sites, where no selectivity is observed [80].

33 Methyl oleate isomerization reactions were also performed at 260°C and 4.0 MPa on H-FER-PAR and
34 H-FER-REC (Fig. 9-B). Consistent with the previously observed behavior at 2MPa, the major products
35 were again the straight double bond positional/geometric isomers of methyl oleate. In the case of H-
36 FER-PAR, the yield of straight C18 isomers reached an even higher value than that obtained at 2 MPa
37 (about 80% vs. about 70%) but the slow increase of the yield with the time-on-stream suggests that
38 diffusional limitations are created during the reaction. The higher maximum yield of branched products
39 (22.0%) obtained at 4.0 MPa compared to the maximum value at 2.0 MPa (8.2%) is coherent with the
40 positive effect of carrier pressure on branching observed on several zeolites [23,78]. However, this
41 yield decreased rapidly after one hour of time on stream, along with the increase in straight C18
42 isomers, probably indicating rapid deactivation of the stronger acidic sites present in the catalyst.

1 In the case of H-FER-REC, the conversion of methyl oleate reached 90 % at the beginning of the reaction
2 but steadily decreased after 3h and reached 64% at 8h time-on-stream. With longer time on stream,
3 partial channel blockage clearly reduces catalyst performance. This can be related to the negative
4 effect of carrier pressure on the stability of the catalyst, observed in olefin isomerization on zeolite
5 HZSM-5 [94]. The yield of straight C18 isomers reached a maximum of 40% after 3h of time-on-stream
6 and then decreased from 40.0% to 28.9%, together with the decrease of conversion. The maximum
7 yield of branched products obtained with recrystallized ferrierite is still higher than in the case of the
8 parent sample, reaching almost 30% after one hour. Then the yields of branched products decrease
9 rapidly with time-on-stream for both parent and recrystallized samples, with a higher residual yield
10 (10%) in the case of H-FER-REC. It appears that the increase in branching activity with pressure also
11 favors oligomerization and byproduct formation, leading to a blockage of active sites, in a trade-off
12 between activity and stability of the catalyst.

13 Finally, methyl oleate isomerization was carried out in a downstream fixed bed continuous flow at
14 285°C and a pressure of 2.0 MPa for several days (Fig. 10) and showed a different behavior than at
15 260°C, regardless of the pressure used. Reactions using both H-FER-PAR and H-FER-REC as catalysts
16 showed higher conversions and yields of branched products under these conditions. Under continuous
17 flow conditions, increasing the temperature from 260°C to 285°C has a significant effect. However, the
18 rapid deactivation of the strong Brønsted acid sites and/or the rapid blocking of the micropores can be
19 observed in the case of H-FER-PAR, as the yield of the branched product rapidly decreased from 30%
20 to 10%, whereas it remained stable at a level of 50% in the case of H-FER-REC. The yields in lactones,
21 oligomers and cracking products showed a similar behavior, with a maximum yield at 10% and a
22 decrease with time on stream in the case of H-FER-PAR. These results show that increasing the
23 temperature to 285°C affect the catalyst stability for H-FER-PAR because it has a more constrained
24 microporous structure in which the coke precursors accumulated more rapidly. In contrast, the
25 positive influence of the mesoporous network in H-FER-REC is evident here, allowing better access to
26 the acidic sites located on the 10-MR channels, leading to the stable yields of branched products
27 observed during the first 8 hours of time-on-stream. However, at this temperature, the production of
28 oligomers increased significantly with the use of H-FER-REC, from 0.8% to 6.7% with time on stream.
29 It has to be observed that compounds previously described in the literature as coke precursors, such
30 as dodecylbenzene [25], which could correspond to what we obtained here, have boiling points close
31 to 285°C. This could increase their diffusion and thus delay the initial formation of coke affecting pore
32 mouth catalysis. In addition, this could explain why the catalytic activity was maintained with time on
33 stream, and why the difference in behavior between 260°C and 285°C is so large. It may delay the
34 complete deactivation of the catalyst under these conditions.



1

2 **Fig. 10** Methyl oleate isomerization in a continuous flow reactor at 285, 310, and 325°C with a return
 3 point at 285°C at a pressure of 2.0 MPa using as the catalyst A. H-FER-PAR. B. H-FER-REC carried out
 4 for 78h.

5 In order to verify that the H-FER-REC maintains this activity for over a longer period of time and at
 6 different temperatures, the raw material flow was reduced to a WHSV of 1.2 h⁻¹ during the nights and
 7 increased back to its working value of 3.5 h⁻¹ during the day while also changing the temperature. Two

1 higher temperatures were tested, 310°C and 325°C, and finally the initial temperature 285°C was
2 tested again to verify the condition and robustness of the catalyst after 78 hours of operation (see Fig.
3 10).

4 After changing the temperature to 310°C and taking samples again, the products obtained did not have
5 the same composition as at 285°C. With increasing temperature, a significant increase in oligomers,
6 cracking products and other by-products was observed, especially on H-FER-REC catalyst. In the case
7 of methyl oleate isomerization using H-FER-PAR (Fig. 10-A), the yield of branched products increased
8 slightly with increasing temperature, as did the yields of lactones and oligomers. This increase in yield
9 of heavier products can be explained by the increase in activity of the unblocked Brønsted acid sites
10 with increasing temperature. However, the yields obtained were lower than those reported in the first
11 hours of time on stream because the catalyst was already largely deactivated. On the other hand, when
12 the reaction was carried out with H-FER-REC as catalyst (Fig. 10-B), a decrease in the yield of branched
13 chain products was observed, while the increase in temperature led to an increase in the yield of
14 lactones and oligomers, as well as the yield of cracking products. The higher amount of other by-
15 products, especially oligomers and cracking products, could lead to the formation of more aromatic
16 precursors, which could explain a lower yield of branched products as it could increase the deactivation
17 of strong acid sites necessary for the isomerization reaction.

18 After the overnight period at low WHSV, the behavior of both catalysts was observed at the same
19 temperature (310°C). As can be seen in Fig. 10 A and B, the conversions in both cases were similar to
20 those of the previous day, showing the stability of the catalyst with a long time on stream. Although
21 the yield of branched products remains almost unchanged with H-FER-PAR as catalyst, a decrease was
22 observed in the case of H-FER-REC, accompanied by a severe increase of cracking products. This
23 indicates that the deactivation of the H-FER-REC catalyst continues. The temperature was then raised
24 to 325°C. For the isomerization of methyl oleate with H-FER-PAR, the yield of branched products was
25 quite stable, as did the yields of lactones and oligomers, but the deactivation of the catalyst continued.
26 This indicates that the number of active Brønsted acid sites of the catalyst decreased and increasing
27 the temperature did not help to reduce it. When H-FER-REC was used as the catalyst, the yield of
28 branched chain products was stable with time-on-flow at the value reached with overnight lower
29 WHSV, although this value was still higher than when the reaction is carried out with H-FER-PAR as the
30 catalyst. Considering that the cracking reactions are favored under these temperature and pressure
31 conditions according to what is published in the literature [27], this increase in temperature led to an
32 increase in cracking products from 20% at 310°C to 30% at 325°C. The major fraction of these gaseous
33 cracking products consisted of low molecular weight hydrocarbons and dimethyl ether. With this in
34 mind, the use of higher temperatures or pressures can lead to hazardous situations with increased
35 production of volatile products. This operating temperature could also lead to an increase in the
36 number of aromatic precursors for coke formation. This is consistent with the significant increase in
37 the amount of oligomers observed.

38 The feed flow was then reduced again overnight and the temperature was changed back to 285°C to
39 evaluate the residual activity of the catalysts at the initial working temperature. Although the
40 conversions were surprisingly high after the overnight period for both H-FER-PAR and H-FER-REC, both
41 catalytic materials showed a rapid decrease with time-on-stream in activity, yields of branched
42 products as well as other by-products. This could be probably related to strong deactivation, which
43 should be studied in more detail.

1 As could be seen, increasing the temperature from 260°C to 285°C had a positive effect. This could be
2 due to greater diffusion of feedstock molecules within the ferrierite framework, as well as greater
3 diffusion of coke precursors, which increases catalytic stability and leads to higher and more stable
4 yields of branched chain C₁₈ methyl ester products with time on stream. Although the higher
5 temperatures of 310 and 325°C maintained high conversions, yields of branched products decreased.
6 In addition, these temperature increases resulted in increased cracking products and oligomer
7 formation.

8 **4. CONCLUSIONS**

9 In order to obtain a ferrierite material with better performance, a mesoporous system of 10-50 nm
10 parallelepiped internal cavities was created by one-step recrystallization using sodium hydroxide and
11 CTAB. This procedure resulted in a hierarchical micromesoporous ferrierite H-FER-REC, with a total
12 acidity lower than that of the parent H-FER-PAR. However, the loss of acidity was mainly due to a
13 nearly complete passivation of Brönsted acid sites in 8-MR by extraframework species and was more
14 than compensated by an increase of Brönsted sites accessible through 10-MR. The large mesopores
15 created could improve the diffusivity of the reactants along the direction of the 10-MR channels and
16 better exploit the internal acidic sites.

17 Under batch conditions, the use of H-FER-REC in the isomerization of methyl oleate resulted in slight
18 improvements in yields of branched products from 58.4% to 59.8% at 260°C and from 55.3% to 62.0%
19 at 285°C. Losses in selectivity typically associated with the loss of some microporosity were not
20 observed in the experiments with H-FER-REC as catalyst because the newly formed mesopores are
21 connected to the outer surface of the zeolite particles by micropores, which may prevent some by-
22 products from leaving until their reconversion. The peculiar constrained mesoporosity of ferrierite
23 allowed a four-times increase of the area of accessible [001] surfaces, providing a remarkable
24 accessibility to the Brönsted sites at the 10-MR pore mouths. Analysis of the spent catalytic materials
25 allowed us to observe that this mesopore system facilitates the transport of coke precursors out of the
26 microporous framework of ferrierite and some of the coke precursors are stored in the constrained
27 mesoporosity, delaying the effects of coking. In addition, analysis of the liquid extract of the spent
28 catalysts allowed us to identify one of the coke precursors as 1-dodecyl-6-methoxycyclohexa-1,3-
29 diene.

30 When methyl isomerization was performed in a downstream fixed bed continuous flow reactor using
31 H-FER-REC as the catalyst, the presence of the mesopore system improved selectivity and stability of
32 the catalyst. In addition, under continuous flow conditions, increasing the temperature from 260°C to
33 285°C had a significant effect. This could be due to a greater diffusion of feedstock molecules within
34 the ferrierite framework and a better diffusion of coke precursors in internal mesopore reservoirs.
35 Improvements due to the use of this micromesopore material as a catalyst and the increase in
36 temperature to 285°C resulted in a continuous flow process that maintained branched product yields
37 of up to 50% with no signs of decline during the first eight hours of time on stream. To the best of our
38 knowledge, this is the first time that the isomerization of methyl oleate has been achieved with a
39 hierarchically porous zeolite in a continuous flow process monitored over more than 3 days, providing
40 valuable insight into the reaction/coking mechanism as well as catalyst behavior and deactivation.

41

1 **ACKNOWLEDGMENTS**

2 The authors thank the National School of Chemistry of Montpellier (ENSCM) for the financial support,
3 and the Charles Gerhardt Institute of Montpellier (ICGM) for the technical support in this project. The
4 authors would like to acknowledge the Chemistry Platform of Campus in Montpellier (University of
5 Montpellier) for the support to do TEM, SEM & EDS experiments. A special acknowledgment to
6 Emmanuel Fernandez and Philippe Gaveau for their help with the NMR analyses. The authors would
7 like to thank Dr. Dariusz Swierczynski, Thomas Cacciaguerra, and Jeremy Rodriguez for their invaluable
8 collaboration in the development of this project.

9
10 **REFERENCES**

- 11 [1] J.O. Metzger, Fats and oils as renewable feedstock for chemistry, *Eur. J. Lipid Sci. Technol.* 111
12 (2009) 865–876. <https://doi.org/10.1002/ejlt.200900130>.
- 13 [2] J.A. Martens, A. Bogaerts, N. De Kimpe, P.A. Jacobs, G.B. Marin, K. Rabaey, M. Saeys, S. Verhelst,
14 The Chemical Route to a Carbon Dioxide Neutral World, *ChemSusChem.* 10 (2017) 1039–1055.
15 <https://doi.org/10.1002/cssc.201601051>.
- 16 [3] Food and Agriculture Organization of the United Nations, FAOSTAT statistical database.
17 <https://search.library.wisc.edu/catalog/999890171702121> (accessed 27 July 2023).
- 18 [4] R. Tesser, R. Vitiello, V. Russo, R. Turco, M. Di Serio, L. Lin, C. Li, Oleochemistry products, in: C. Li,
19 Z. Xiao, L. He, M. Di Serio, X. Xie (Eds), *Industrial Oil Plant*, Springer, Singapore, 2020, pp.201-268.
20 <https://doi.org/10.1007/978-981-15-4920-5>.
- 21 [5] A. Masudi, O. Muraza, Vegetable Oil to Biolubricants: Review on Advanced Porous Catalysts,
22 *Energy Fuels* 32 (2018) 10295–10310. <https://doi.org/10.1021/acs.energyfuels.8b02017>.
- 23 [6] K. Hill, Fats and Oils as Oleochemical Raw Materials, *Pure Appl. Chem.* 72 (2000) 1255–1264.
24 <https://doi.org/10.5650/jos.50.433>.
- 25 [7] A. Bohlouli, L. Mahdavian, Catalysts used in biodiesel production: a review, *Biofuels-UK* 0 (2019)
26 1–14. <https://doi.org/10.1080/17597269.2018.1558836>.
- 27 [8] A. Amin, Review of diesel production from renewable resources: Catalysis, process kinetics and
28 technologies, *Ain Shams Eng. J.* 10 (2019) 821–839. <https://doi.org/10.1016/j.asej.2019.08.001>.
- 29 [9] S. Patnaik, S. Martha, K.M. Parida, An overview of the structural, textural and morphological
30 modulations of g-C₃N₄ towards photocatalytic hydrogen production, *RSC Adv.* 6 (2016) 46929–
31 46951. <https://doi.org/10.1039/C5RA26702A>.
- 32 [10] K. Albrecht, R. Hallen, A Brief Literature Overview of Various Routes to Biorenewable Fuels from
33 Lipids for the National Alliance for Advanced Biofuels and Bio-products (NAABB) Consortium,
34 Richland, WA: Pacific Northwest National Laboratory, 2011.
35 [https://www.pnnl.gov/publications/brief-literature-overview-various-routes-biorenewable-](https://www.pnnl.gov/publications/brief-literature-overview-various-routes-biorenewable-fuels-lipids-national-alliance)
36 [fuels-lipids-national-alliance](https://www.pnnl.gov/publications/brief-literature-overview-various-routes-biorenewable-fuels-lipids-national-alliance).
- 37 [11] C. Renee, A novel bifunctional catalyst for alkene isomerization : development, scope and
38 limitations, and applications in organic transformations, PhD thesis, University of California,
39 2012, <https://escholarship.org/uc/item/61q7f7j4>.
- 40 [12] A. Dhar, R.L. Vekariya, P. Bhadja, n-Alkane isomerization by catalysis-a method of industrial
41 importance: An overview, *Cogent Chem.* 4 (2018) 1-19.
42 <https://doi.org/10.1080/23312009.2018.1514686>.
- 43 [13] Q. Yu, Y.-X. Ma, Z. Qin, X.-R. Luo, H.-M. Liu, X.-D. Wang, Using solid acid catalysts to improve the
44 oxidative stability of cold-pressed sesame oil, *LWT-Food Sci. Technol.* 141 (2021) 110928.
45 <https://doi.org/10.1016/j.lwt.2021.110928>.
- 46 [14] U. Biermann, J.O. Metzger, Synthesis of alkyl-branched fatty acids, *Eur. J. Lipid Sci. Technol.* 110
47 (2008) 805–811. <https://doi.org/10.1002/ejlt.200800033>.

- 1 [15] M.I. Sarker, R.J. Latona, R.A. Moreau, D. Micheroni, K.C. Jones, H.L. Ngo, Convenient and
2 Environmentally Friendly Production of Isostearic Acid with Protonic Forms of Ammonium
3 Cationic Zeolites, *Eur. J. Lipid Sci. Technol.* 119 (2017) 1700262.
4 <https://doi.org/10.1002/ejlt.201700262>.
- 5 [16] S.C.C. Wiedemann, P.C.A. Bruijninx, B.M. Weckhuysen, Isostearic Acid: A Unique Fatty Acid with
6 Great Potential, in: F. Cavani, S. Albonetti, F. Basile, A. Gandini (Eds), *Chemicals and Fuels from*
7 *Bio-Based Building Blocks*, Wiley-VCH, Weinheim, 2016, pp. 51–78.
8 <https://doi.org/10.1002/9783527698202.ch3>.
- 9 [17] U. Biermann, U.T. Bornscheuer, I. Feussner, M.A.R. Meier, J.O. Metzger, Fatty Acids and their
10 Derivatives as Renewable Platform Molecules for the Chemical Industry, *Angew. Chem.-Int. Edit.*
11 60 (2021) 20144–20165. <https://doi.org/10.1002/anie.202100778>.
- 12 [18] G. Dabrowski, I. Konopka, Update on food sources and biological activity of odd-chain, branched
13 and cyclic fatty acids — A review, *Trends Food Sci. Technol.* 119 (2022) 514–529.
14 <https://doi.org/10.1016/j.tifs.2021.12.019>.
- 15 [19] G. Biresaw, H.L. Ngo, R.O. Dunn, Investigation of the Physical and Tribological Properties of Iso -
16 Oleic Acid, *JAOCS, J. Am. Oil Chem. Soc.* 96 (2019) 189–199. <https://doi.org/10.1002/aocs.12177>.
- 17 [20] J. Habelberg, A. Behr, Saturated branched fatty compounds: Proven industrial processes and new
18 alternatives, *Eur. J. Lipid Sci. Technol.* 118 (2016) 36–46. <https://doi.org/10.1002/ejlt.201500461>.
- 19 [21] H.L. Ngo, A. Nuñez, W. Lin, T. a. Foglia, A. Nunez, W. Lin, T. a. Foglia, Zeolite-catalyzed
20 isomerization of oleic acid to branched-chain isomers, *Eur. J. Lipid Sci. Technol.* 109 (2007) 214–
21 224. <https://doi.org/10.1002/ejlt.200600246>.
- 22 [22] R.O. Dunn, H.L. Ngo, M.J. Haas, Branched-Chain Fatty Acid Methyl Esters as Cold Flow Improvers
23 for Biodiesel, *J. Am. Oil Chem. Soc.* 92 (2015) 853–869. <https://doi.org/10.1007/s11746-015-2643-2>.
- 24 [23] S.J. Reaume, N. Ellis, Optimizing Reaction Conditions for the Isomerization of Fatty Acids and
25 Fatty Acid Methyl Esters to Their Branch Chain Products, *J. Am. Oil Chem. Soc.* 88 (2011) 661–
26 671. <https://doi.org/10.1007/s11746-010-1718-3>.
- 27 [24] J.F. Sierra-Cantor, C.A. Guerrero-Fajardo, Methods for improving the cold flow properties of
28 biodiesel with high saturated fatty acids content : A review, *Renew. Sust. Energ. Rev.* 72 (2017)
29 774–790. <https://doi.org/10.1016/j.rser.2017.01.077>.
- 30 [25] S.C.C. Wiedemann, J.A. Stewart, F. Soulimani, T. Van Bergen-Brenkman, S. Langelaar, B. Wels, P.
31 De Peinder, P.C.A. Bruijninx, B.M. Weckhuysen, Skeletal isomerisation of oleic acid over
32 ferrierite in the presence and absence of triphenylphosphine: Pore mouth catalysis and related
33 deactivation mechanisms, *J. Catal.* 316 (2014) 24–35.
34 <https://doi.org/10.1016/j.jcat.2014.04.018>.
- 35 [26] G. Biresaw, Y. Chen, L. Chen, H. Ngo, K. Wagner, K.E. Vermillion, S.C. Cermak, Iso-oleic estolide
36 products with superior cold flow properties, *Ind. Crop. Prod.* 182 (2022) 114857.
37 <https://doi.org/10.1016/j.indcrop.2022.114857>.
- 38 [27] J. Weitkamp, Catalytic Hydrocracking-Mechanisms and Versatility of the Process, *ChemCatChem.*
39 4 (2012) 292–306. <https://doi.org/10.1002/cctc.201100315>.
- 40 [28] R. Maghrebi, M. Buffi, P. Bondioli, D. Chiaramonti, 2021. Isomerization of long-chain fatty acids
41 and long-chain hydrocarbons: A review. *Renew. Sust. Energ. Rev.* 149, 111264.
42 <https://doi.org/10.1016/j.rser.2021.111264>
- 43 [29] A.F. Elsasser, L.A. McCargar, Method of preparing dimeric fatty acids and/or esters thereof
44 containing low residual interesters and the resulting dimeric fatty acids and/or dimeric fatty
45 esters, patent WO0109066, 8 Feb 2001.
- 46 [30] M.I. Sarker, R.A. Moreau, H.L. Ngo, Comparison of Various Phosphine Additives in Zeolite Based
47 Catalytic Isomerization of Oleic Acid, *Eur. J. Lipid Sci. Technol.* (2018).
48 <https://doi.org/10.1002/ejlt.201800070>.
- 49 [31] H.L. Ngo, E. Hoh, T. a. Foglia, Improved synthesis and characterization of saturated branched-
50 chain fatty acid isomers, *Eur. J. Lipid Sci. Technol.* 114 (2012) 213–221.
51 <https://doi.org/10.1002/ejlt.201000471>.
- 52

- 1 [32] J.C. Yori, M.A. D'Amato, J.M. Grau, C.L. Pieck, C.R. Vera, Depression of the cloud point of biodiesel
2 by reaction over solid acids, *Energy Fuels* 20 (2006) 2721–2726.
3 <https://doi.org/10.1021/ef060245i>.
- 4 [33] W.R. Hodgson, W. Tijmen, C. Lok, G. Roberts, Fatty acid isomerisation, patent US005856539A, 5
5 Jan 1999.
- 6 [34] L. Ha, J. Mao, J. Zhou, Z.C. Zhang, S. Zhang, Skeletal isomerization of unsaturated fatty acids on
7 Beta zeolites: Effects of calcination temperature and additives, *Appl. Catal. A-Gen.* 356 (2009)
8 52–56. <https://doi.org/10.1016/j.apcata.2008.12.018>.
- 9 [35] S. Zhang, Z. Zhang, D. Steichen, Skeletal Isomerization of Fatty Acids, patent US2003100780, 29
10 May 2003.
- 11 [36] J. Zhang, J. Uknalis, L. Chen, R.A. Moreau, H.L. Ngo, Development of Magnesium Oxide–Zeolite
12 Catalysts for Isomerization of Fatty Acids, *Catal. Lett.* 149 (2019) 303–312.
13 <https://doi.org/10.1007/s10562-018-2601-3>.
- 14 [37] A. Bolshakov, R. van de Poll, T. van Bergen-Brenkman, S.C.C. Wiedemann, N. Kosinov, E.J.M.
15 Hensen, Hierarchically porous FER zeolite obtained via FAU transformation for fatty acid
16 isomerization, *Appl. Catal. B-Environ.* 263 (2019) 118356.
17 <https://doi.org/10.1016/j.apcatb.2019.118356>.
- 18 [38] S. Zhang, Z.C. Zhang, Skeletal isomerization of unsaturated fatty acids: the role of mesopores in
19 HBeta zeolites, *Catal. Lett.* 115 (2007) 114–121. <https://doi.org/10.1007/s10562-007-9083-z>.
- 20 [39] S. Mardiana, J.A. Azhari, G.T.M. Kadja, On the Effectiveness of Hierarchical Zeolite Catalyst for
21 Isomerization of Biomass-Derived Compound, *Journal of Research and Development on
22 Nanotechnology.* 1 (2021) 23–27. <https://doi.org/10.5614/jrdn.2021.1.1.16619>
- 23 [40] D. Kerstens, H. De Peuter, I. Khalil, S. Van Praet, J. Van Aelst, B.F. Sels, Fast and Selective Solvent-
24 Free Branching of Unsaturated Fatty Acids with Hierarchical ZSM-5, *ACS Sustain. Chem. Eng.* 9
25 (2021) 4357–4362. <https://doi.org/10.1021/acssuschemeng.0c09161>
- 26 [41] J. García-Martínez, K. Li, Mesoporous Zeolites: Preparation, Characterization, and Applications,
27 Wiley-VHC, Weinheim, 2015. <https://doi.org/10.1002/9783527673957>.
- 28 [42] D. Verboekend, N. Nuttens, R. Locus, J. Van Aelst, P. Verolme, J.C. Groen, J. Pérez-Ramírez, B.F.
29 Sels, Synthesis, characterisation, and catalytic evaluation of hierarchical faujasite zeolites:
30 Milestones, challenges, and future directions, *Chem. Soc. Rev.* 45 (2016) 3331–3352.
31 <https://doi.org/10.1039/c5cs00520e>.
- 32 [43] X. Cheng, T. Cacciaguerra, D. Minoux, J.P. Dath, F. Fajula, C. Gérardin, Generation of
33 parallelepiped-shaped mesopores and structure transformation in highly stable ferrierite zeolite
34 crystals by framework desilication in NaOH solution, *Micropor. Mesopor. Mat.* 260 (2018) 132–
35 145. <https://doi.org/10.1016/j.micromeso.2017.05.050>.
- 36 [44] B. Gil, S.I. Zones, S.J. Hwang, M. Bejblová, J. Čejka, Acidic properties of SSZ-33 and SSZ-35 novel
37 zeolites: A complex infrared and MAS NMR study, *J. Phys. Chem. C* 112 (2008) 2997–3007.
38 <https://doi.org/10.1021/jp077687v>.
- 39 [45] I.I. Ivanova, I.A. Kasyanov, A.A. Maerle, V.I. Zaikovskii, Mechanistic study of zeolites
40 recrystallization into micro-mesoporous materials, *Microporous Mesoporous Mat.* 189 (2014)
41 163–172. <https://doi.org/10.1016/j.micromeso.2013.11.001>.
- 42 [46] A. Sachse, A. Grau-Atienza, E.O. Jardim, N. Linares, M. Thommes, J. García-Martínez,
43 Development of Intracrystalline Mesoporosity in Zeolites through Surfactant-Templating, *Cryst.
44 Growth Des.* 17 (2017) 4289–4305. <https://doi.org/10.1021/acs.cgd.7b00619>.
- 45 [47] I.I. Ivanova, E.E. Knyazeva, Micro-mesoporous materials obtained by zeolite recrystallization:
46 Synthesis, characterization and catalytic applications, *Chem. Soc. Rev.* 42 (2013) 3671–3688.
47 <https://doi.org/10.1039/c2cs35341e>.
- 48 [48] A.G. Pelmenschikov, R.A. Van Santen, J. Jänchen, E. Meijer, CD3CN as a probe of Lewis and
49 Bronsted acidity of zeolites, *J. Phys. Chem.* 97 (1993) 11071–11074.
50 <https://doi.org/10.1021/j100144a028>.

- 1 [49] T.M. Davis, C.Y. Chen, N. Žilková, D. Vitvarová-Procházková, J. Čejka, S.I. Zones, The importance
2 of channel intersections in the catalytic performance of high silica stilbite, *J. Catal.* 298 (2013)
3 84–93. <https://doi.org/10.1016/j.jcat.2012.10.022>.
- 4 [50] R. Rachwalik, M. Hunger, B. Sulikowski, Transformations of monoterpene hydrocarbons on
5 ferrierite type zeolites, *Appl. Catal. A-Gen.* 427–428 (2012) 98–105.
6 <https://doi.org/10.1016/j.apcata.2012.03.037>.
- 7 [51] V.L. Zholobenko, D.B. Lukyanov, J. Dwyer, W.J. Smith, Ferrierite and SUZ-4 zeolite:
8 Characterization of acid sites, *J. Phys. Chem. B* 102 (1998) 2715–2721.
9 <https://doi.org/10.1021/jp973340o>.
- 10 [52] K. Chakarova, K. Hadjiivanov, FTIR study of N₂ and CO adsorption on H-D-FER, Microporous and
11 Mesoporous Materials. 177 (2013) 59–65. <https://doi.org/10.1016/j.micromeso.2013.04.022>.
- 12 [53] S. Bordiga, C. Lamberti, F. Bonino, A. Travert, F. Thibault-Starzyk, Probing zeolites by vibrational
13 spectroscopies, *Chem. Soc. Rev.* 44 (2015) 7262–7341. <https://doi.org/10.1039/c5cs00396b>.
- 14 [54] C. Pazé, A. Zecchina, S. Spera, G. Spano, F. Rivetti, Acetonitrile as probe molecule for an
15 integrated 1H NMR and FTIR study of zeolitic Brønsted acidity: Interaction with zeolites H-
16 ferrierite and H-beta, *Phys. Chem. Chem. Phys.* 2 (2000) 5756–5760.
17 <https://doi.org/10.1039/B005677O>.
- 18 [55] P.G. Rouxhet, R.E. Sempels, Hydrogen Bond Strengths and Acidities of Hydroxyl groups on
19 Silica-Alumina Surfaces and in Molecules in Solution, *J. Chem. Soc. Faraday Trans.* 170 (1974)
20 2021–2032. <https://doi.org/10.1039/F19747002021>
- 21 [56] R.E. Sempel, P.G. Rouxhet, Infrared Study of the Adsorption of Benzene and Acetonitrile on
22 Silica-Alumina Gels: Acidity Properties and Surface Heterogeneity, *J. Colloid Interface Sci.* 55
23 (1976) 263–273. [https://doi.org/10.1016/0021-9797\(76\)90033-3](https://doi.org/10.1016/0021-9797(76)90033-3)
- 24 [57] W. Daniell, N.Y. Topsøe, H. Knözinger, An FTIR study of the surface acidity of USY zeolites:
25 Comparison of CO, CD₃CN, and C₅H₅N probe molecules, *Langmuir* 17 (2001) 6233–6239.
26 <https://doi.org/10.1021/la010345a>.
- 27 [58] R. Rachwalik, Z. Olejniczak, B. Sulikowski, Dealumination of ferrierite type zeolite:
28 Physicochemical and catalytic properties, *Catal. Today* 101 (2005) 147–154.
29 <https://doi.org/10.1016/j.cattod.2005.01.012>.
- 30 [59] E. Catizzzone, M. Migliori, T. Mineva, S. van Daele, V. Valtchev, G. Giordano, New synthesis routes
31 and catalytic applications of ferrierite crystals. Part 2: The effect of OSDA type on zeolite
32 properties and catalysis, *Micropor. Mesopor. Mat.* 296 (2020) 109988.
33 <https://doi.org/10.1016/j.micromeso.2019.109988>.
- 34 [60] A.A. Belhekar, R.K. Ahedi, S. Kuriyavar, S.S. Shevade, B.S. Rao, R. Anand, Z. Tvaruzkova, Effect of
35 acid sites of Al- and Fe-Ferrierite on m-xylene isomerization, *Catal. Commun.* 4 (2003) 295–302.
36 [https://doi.org/10.1016/S1566-7367\(03\)00056-6](https://doi.org/10.1016/S1566-7367(03)00056-6).
- 37 [61] B. Wichterlova, Z. Tvaruzkova, Z. Sobalik, P. Sarv, Determination and properties of acid sites in H-
38 ferrierite. A comparison of ferrierite and MFI structures. *Micropor. Mesopor. Mat.* 24 (1998) 223–
39 233. [https://doi.org/10.1016/S1387-1811\(98\)00167-X](https://doi.org/10.1016/S1387-1811(98)00167-X)
- 40 [62] L. Kubelková, J. Kotrla, J. Florián. H-Bonding and Interaction Energy of Acetonitrile Neutral and
41 Pyridine Ion-Pair Surface Complexes in Zeolites of Various Acidity: FTIR and ab Initio Study. *J.*
42 *Phys. Chem.* 99 (1995) 10285–10293. <https://doi.org/10.1021/j100025a033>
- 43 [63] M. Rubes, M. Trachta, J. Vaculík, R. Bulanek, O. Bludský. The analysis of the BAS OH band in
44 zeolites. *Micropor. Mesopor. Mat.* 341 (2022) 112052.
45 <https://doi.org/10.1016/j.micromeso.2022.112052>
- 46 [64] A. Alberti, A. Martucci. Proton Transfer Mediated by Water: Experimental Evidence by Neutron
47 Diffraction. *J. Phys. Chem. C* 114 (2010) 7767–7773. <https://doi.org/10.1021/jp100370u>
- 48 [65] E.G. Fuentes-Ordóñez, J.A. Salbidegoitia, J.L. Ayastuy, M.A. Gutiérrez-Ortiz, M.P. González-
49 Marcos, J.R. González-Velasco, High external surface Pt/zeolite catalysts for improving
50 polystyrene hydrocracking, *Catal. Today.* 227 (2014) 163–170.
51 <https://doi.org/10.1016/j.cattod.2013.09.004>.

- 1 [66] W.J. Roth, B. Gil, A. Mayoral, J. Grzybek, A. Korzeniowska, M. Kubu, W. Makowski, J. Čejka, Z.
2 Olejniczak, M. Mazur, Pillaring of layered zeolite precursors with ferrierite topology leading to
3 unusual molecular sieves on the micro/mesoporous border, *Dalton Trans.* 47 (2018) 3029–3037.
4 <https://doi.org/10.1039/c7dt03718j>.
- 5 [67] X. Niu, Y. Song, S. Xie, S. Liu, Q. Wang, L. Xu, Synthesis and catalytic reactivity of MCM-22/ZSM-
6 35 composites for olefin aromatization, *Catal. Lett.* 103 (2005) 211–218.
7 <https://doi.org/10.1007/s10562-005-7156-4>.
- 8 [68] S. Xie, S. Liu, Y. Liu, X. Li, W. Zhang, L. Xu, Synthesis and characterization of MCM-49/ZSM-35
9 composite zeolites in the hexamethyleneimine and cyclohexamine system, *Micropor. Mesopor.*
10 *Mat.* 121 (2009) 166–172. <https://doi.org/10.1016/j.micromeso.2009.01.027>.
- 11 [69] E. Koohsaryan, M. Anbia, Nanosized and hierarchical zeolites: A short review, *Chin. J. Catal.* 37
12 (2016) 447–467. [https://doi.org/10.1016/S1872-2067\(15\)61038-5](https://doi.org/10.1016/S1872-2067(15)61038-5).
- 13 [70] Y.P. Khitev, Y.G. Kolyagin, I.I. Ivanova, O.A. Ponomareva, F. Thibault-Starzyk, J.-P. Gilson, C.
14 Fernandez, F. Fajula, Synthesis and catalytic properties of hierarchical micro/mesoporous
15 materials based on FER zeolite, *Micropor. Mesopor. Mat.* 146 (2011) 201–207.
16 <https://doi.org/10.1016/j.micromeso.2011.05.003>.
- 17 [71] D. Li, Y. Chen, J. Hu, B. Deng, X. Cheng, Y. Zhang. Synthesis of Hierarchical Chabazite Zeolite via
18 Interzeolite Transformation of Coke-containing Spent MFI. *Appl. Catal. B-Environ.* 270 (2020)
19 118881. <https://doi.org/10.1016/j.apcatb.2020.118881>
- 20 [72] Y.P. Khitev, I.I. Ivanova, Y.G. Kolyagin, O.A. Ponomareva, Skeletal isomerization of 1-butene over
21 micro/mesoporous materials based on FER zeolite, *Appl. Catal. A-Gen.* 441–442 (2012) 124–135.
22 <https://doi.org/10.1016/j.apcata.2012.07.010>.
- 23 [73] H.L. Ngo, R.O. Dunn, E. Hoh, C₁₈-unsaturated branched-chain fatty acid isomers: Characterization
24 and physical properties, *Eur. J. Lipid Sci. Technol.* 115 (2013) 676–683.
25 <https://doi.org/10.1002/ejlt.201200323>.
- 26 [74] S.C.C. Wiedemann, A. Muñoz-Murillo, R. Oord, T. Van Bergen-Brenkman, B. Wels, P.C. a.
27 Bruijninx, B.M. Weckhuysen, Skeletal isomerisation of oleic acid over ferrierite: Influence of acid
28 site number, accessibility and strength on activity and selectivity, *J. Catal.* 329 (2015) 195–205.
29 <https://doi.org/10.1016/j.jcat.2015.05.013>.
- 30 [75] G. Knothe, R.O. Dunn, A Comprehensive Evaluation of the Melting Points of Fatty Acids and Esters
31 Determined by Differential Scanning Calorimetry, *J. Am. Oil Chem. Soc.* 86 (2009) 843–856.
32 <https://doi.org/10.1007/s11746-009-1423-2>.
- 33 [76] H.L. Ngo, Lewis base additives improve the zeolite Ferrierite-catalyzed synthesis of isostearic
34 acids synthesis of isostearic acids, *J. Am. Oil Chem. Soc.* 92 (2015) 613–619.
35 <https://doi.org/10.1007/s11746-015-2608-5>.
- 36 [77] M. Fan, T. Si, P. Zhang, Effect of Surface Modification of H⁺-Mordenite on the Isomerization of
37 Oleic Acid into Branched-Chain Isomers, *J. Am. Oil Chem. Soc.* 95 (2018) 1357–1365.
38 <https://doi.org/10.1002/aocs.12142>.
- 39 [78] A. Ferreira Young, P. Nothaft Romano, J. Monnerat Araújo Ribeiro de Almeida, D. A. Gomes
40 Aranda. Isomerization of Oleic Acid over Acid Zeolites: Design of Experiments and Proposal of a
41 Novel Kinetic Mechanism. *Ind. Eng. Chem. Res.* 60 (2021) 14051–14059.
42 <https://doi.org/10.1021/acs.iecr.1c02054>
- 43 [79] S.C.C. Wiedemann, Z. Ristanović, G.T. Whiting, V.R. Reddy Marthala, J. Kärger, J. Weitkamp, B.
44 Wels, P.C.A. Bruijninx, B.M. Weckhuysen, Large Ferrierite Crystals as Models for Catalyst
45 Deactivation during Skeletal Isomerisation of Oleic Acid: Evidence for Pore Mouth Catalysis,
46 *Chem.-Eur. J.* 22 (2016) 199–210. <https://doi.org/10.1002/chem.201503551>.
- 47 [80] J. Houžvička, V. Ponec. Skeletal isomerisation of n-butene on phosphorus containing catalysts.
48 *Appl. Catal. A: Gen.* 145 (1996) 95–109. [https://doi.org/10.1016/0926-860X\(96\)00144-5](https://doi.org/10.1016/0926-860X(96)00144-5)
- 49 [81] R. Chal, C. Gerardin, M. Bulut, S. Van Donk, Overview and Industrial Assessment of Synthesis
50 Strategies towards Zeolites with Mesopores, *ChemCatChem.* 3 (2011) 67–81.
51 <https://doi.org/10.1002/cctc.201000158>.

- 1 [82] R. Srivastava, Synthesis and applications of ordered and disordered mesoporous zeolites: Present
2 and future prospective, *Catal. Today.* 309 (2018) 172–188.
3 <https://doi.org/10.1016/j.cattod.2017.08.017>.
- 4 [83] H.L. Ngo, T.A. Foglia, Process for preparing saturated branched chained fatty acids, patent
5 US2011275844, 10 Nov 2011.
- 6 [84] D. Verboekend, New Hierarchical Zeolite Catalysts by Post-Synthetic Design, PhD thesis, ETH
7 Zurich, 2012. <https://doi.org/10.3929/ethz-a-007595445>.
- 8 [85] L. Vaugon, Etude des performances en hydrocraquage de catalyseurs zéolithiques modèles :
9 influence de l'architecture poreuse et de l'acidité, PhD thesis, ENSCM, Montpellier, 2017.
10 <https://www.theses.fr/2017ENCM0015>
- 11 [86] S. Van Donk, Adsorption, Diffusion and Reaction Studies of Hydrocarbons on Zeolite Catalysts,
12 PhD thesis Utrecht university, 2002. <https://dspace.library.uu.nl/handle/1874/764>
- 13 [87] S.C.C. Wiedemann, Ferrierite-Catalysed Branching of Unsaturated Fatty Acids, PhD thesis, Utrech
14 University, 2015. <https://dspace.library.uu.nl/handle/1874/324940>
- 15 [88] S. Hamieh, Transformation des alcools sur zéolithes protoniques : “rôle paradoxal du coke”, PhD
16 thesis, University of Poitiers, 2013. [http://nuxeo.edel.univ-
17 poitiers.fr/nuxeo/site/esupversions/c9b0cca1-c5f5-4304-98b6-10e76e998104](http://nuxeo.edel.univ-poitiers.fr/nuxeo/site/esupversions/c9b0cca1-c5f5-4304-98b6-10e76e998104)
- 18 [89] H.S. Cerqueira, C. Sievers, G. Joly, P. Magnoux, J.A. Lercher, Multitechnique characterization of
19 coke produced during commercial resid FCC operation, *Ind. Eng. Chem. Res.* 44 (2005) 2069–
20 2077. <https://doi.org/10.1021/ie048963k>.
- 21 [90] C.E. Snape, B.J. McGhee, S.C. Martin, J.M. Andresen, Structural characterisation of catalytic coke
22 by solid-state ¹³C-NMR spectroscopy, *Catal. Today.* 37 (1997) 285–293.
23 [https://doi.org/10.1016/S0920-5861\(97\)00021-7](https://doi.org/10.1016/S0920-5861(97)00021-7).
- 24 [91] M.A. Callejas, M.T. Martínez, T. Blasco, E. Sastre, Coke characterisation in aged residue
25 hydrotreating catalysts by solid-state ¹³C-NMR spectroscopy and temperature-programmed
26 oxidation, *Appl. Catal. A-Gen.* 218 (2001) 181–188. [https://doi.org/10.1016/S0926-
27 860X\(01\)00640-8](https://doi.org/10.1016/S0926-860X(01)00640-8).
- 28 [92] A. Devaraj, M. Vijayakumar, J. Bao, M.F. Guo, M.A. Derewinski, Z. Xu, M.J. Gray, S. Prodingler, K.K.
29 Ramasamy, 2016. Discerning the Location and Nature of Coke Deposition from Surface to Bulk of
30 Spent Zeolite Catalysts. *Sci. Rep.* 6 (2016) 37586. <https://doi.org/10.1038/srep37586>.
- 31 [93] M. Kondratiuk, D. Gopinath, A. Elrrays, L.J. Gooßen, Double-Bond Isomerization of Rapeseed Oil
32 Methyl Esters in a Continuous Flow Reactor Efficiently Catalyzed by H-Mordenite, *Eur. J. Lipid Sci.*
33 *Technol.* 125 (2023) 2200163. <https://doi.org/10.1002/ejlt.202200163>.
- 34 [94] M. Díaz, E. Epelde, A. T. Aguayo, J. Bilbao. Low-pressure oligomerization of 1-butene to liquid
35 fuels on HZSM-5. zeolite catalysts: Effect of operating conditions. *J. Ind. Eng. Chem.* 87 (2020)
36 234–241. <https://doi.org/10.1016/j.jiec.2020.04.006>.